Three-dimensional Martian Ionosphere model: I. The photochemical ionosphere below 180 km

F. González-Galindo, Jean-Yves Chaufray, M. A. López-Valverde, G. Gilli, François Forget, François Leblanc, Ronan Modolo, Sebastien Hess, M. Yagi

JOURNAL OF GEOPHYSICAL RESEARCH: PLANETS, VOL. 118, 2105–2123, doi:10.1002/jgre.20150, 2013

Three-dimensional Martian ionosphere model: I. The photochemical ionosphere below 180 km

F. González-Galindo,[1] J.-Y. Chaufray,[2,3] M. A. López-Valverde,[1] G. Gilli,[1] F. Forget,[2] F. Leblanc,[3] R. Modolo,[3] S. Hess,[3] and M. Yagi[3]

Received 16 May 2013; revised 5 August 2013; accepted 31 August 2013; published 8 October 2013.

[1] We describe the Mars ionosphere with unprecedented detail in 3-D, as simulated by a Mars general circulation model (the Laboratoire de Météorologie Dynamique Mars GCM), and compare it with recent measurements. The model includes a number of recent extensions and improvements. Different simulations for a full Martian year have been performed. The electron density at the main ionospheric peak is shown to vary with the Sun-Mars distance and with the solar variability, both in the long-term (11 year solar cycle) and on shorter temporal scales (solar rotation). The main electronic peak is shown to be located at the same pressure level during all the Martian year. As a consequence, its altitude varies with latitude, local time, and season according to the natural expansions and fluctuations of the neutral atmosphere, in agreement with previous models. The model predicts a nighttime ionosphere due only to photochemistry. The simulated ionosphere close to the evening terminator is in agreement with observations. No effort has been made to explain the patchy ionosphere observed in the deep nightside. We have compared the modeled ionosphere with Mars Global Surveyor and Mars Advanced Radar for Subsurface and Ionosphere Sounding data. The model reproduces the solar zenith angle variability of the electron density and the altitude of the peak, although it underestimates the electron density at the main peak by about 20%. The electron density at the secondary peak is strongly underestimated by the model, probably due to a very crude representation of the X-ray solar flux. This is one of the aspects that needs a revision in future versions of the model.

Citation: González-Galindo, F., J.-Y. Chaufray, M. A. López-Valverde, G. Gilli, F. Forget, F. Leblanc, R. Modolo, S. Hess, and M. Yagi (2013), Three-dimensional Martian ionosphere model: I. The photochemical ionosphere below 180 km, *J. Geophys. Res. Planets*, *118*, 2105–2123, doi:10.1002/jgre.20150.

1. Introduction

[2] The Martian ionosphere has been subject of study since the first missions to the red planet. In the last decade, three different instruments, the Mars Global Surveyor (MGS) Radio Science Subsystem (RSS), the Mars Radio Science Experiment (MaRS) and the Mars Advanced Radar for Subsurface and Ionosphere Sounding (MARSIS), both on board Mars Express (MEx), have sounded this atmospheric region, revealing its main features. While above about 180–200 km the structure of the ionosphere is controlled mainly by plasma dynamics, below that altitude the timescale for plasma transport is much longer than the chemical timescale, and plasma dynamics can be neglected [*Schunk and Nagy*, 2009]. The photochemistry-driven ionosphere below about 200 km consists mostly of O_2^+, as shown by Viking measurements [*Hanson et al.*, 1977]. The primary peak in electron density occurs at about 130 km altitude and is known as the M2 layer (analogous to the terrestrial F1 layer). A secondary peak occurs around 100 km and is called the M1 layer (analogous to the terrestrial E layer) [e.g., *Withers*, 2009]. Models of the ionosphere [e.g., *Fox et al.*, 1996] have shown that the primary peak is produced mainly by absorption of EUV radiation between 10 and 100 nm, while the secondary peak is originated by more energetic radiation and by photoelectron impact ionization. A sporadic third layer formed by the ablation of meteors in the Martian atmosphere has also been detected [*Pätzold et al.*, 2005; *Withers et al.*, 2008]. This layer is beyond the scope of our work at present.

[3] The different sources of variability of the Martian ionosphere have been studied using data from different spacecraft. A recent review [*Withers*, 2009] compiles the different observations. The best known variability is that affecting the main ionospheric peak. It has been shown [e.g., *Fox and Yeager*, 2009; *Morgan et al.*, 2008; *Němec et al.*,

[1]Instituto de Astrofísica de Andalucía, CSIC, Granada, Spain.
[2]Laboratoire de Météorologie Dynamique, Université Paris VI, Paris, France.
[3]Laboratoire Atmosphère, Milieux et Observations Spatiales, IPSL/UVSQ/Université Paris VI, Paris, France.

Corresponding author: F. González-Galindo, Instituto de Astrofísica de Andalucía, CSIC, Glorieta de la Astronomía, s/n, Granada 18008, Spain. (ggalindo@iaa.es)

2169-9097/13/10.1002/jgre.20150

2011] that the peak electron density varies with solar zenith angle (SZA) following the expected behavior of a Chapman layer, except for high values of SZA (close to 90°). It has also been observed that the peak electron density is strongly influenced by the solar activity [*Nielsen et al.*, 2006; *Morgan et al.*, 2008; *Fox and Yeager*, 2009] and the presence of magnetic fields [*Nielsen et al.*, 2007]. In particular, the analysis of MARSIS data showed a significant increase of the peak electron density and a peak altitude about 20 km lower than usual over regions of intense crustal field, attributed to an increase of the electron temperature [*Nielsen et al.*, 2007; *Gurnett et al.*, 2008]. Different measurements have also shown that the Martian ionosphere is strongly influenced by the underlying neutral atmosphere. In particular, the altitude of the main ionospheric peak varies with longitude for fixed latitude, local time, solar zenith angle (SZA hereafter), and season, due to a similar variation in the neutral density [*Bougher et al.*, 2001, 2004]. It has also been shown that the presence of global dust storms lifts the altitude of the main ionospheric peak [*Hantsch and Bauer*, 1990]. A recent study using MaRS data [*Withers et al.*, 2012a] shows the complexity and variability of the vertical structure of the Martian ionosphere. The different factors influencing the ionosphere close to the terminator and in the nightside have been summarized in *Lillis et al.* [2009]. These include the variability of the neutral atmosphere, the day-night plasma transport, the effects of temperature on recombination rates, transient events, effects of precipitating particles, and the variability of the magnetic field.

[4] While observations are the key stone in our knowledge of the Martian ionosphere, they have inherent limitations in their temporal and geographical coverage. Computational models can help to overcome these limitations and in addition provide further insight into the physical processes that produce the observed structures. Most of the ionospheric models for Mars are 1-D, that is, they only consider variations with altitude. They have the advantage of being computationally fast, which allows them to treat in detail some processes that are too CPU-intensive to be included without approximations in multidimensional models. On the other hand, they neglect the horizontal transport and they usually consider a fixed neutral atmosphere (temperature, density, and composition) as an input to the ionospheric model, which prevents these models from studying the effects of the variations of the neutral atmosphere over the ionosphere. Recently, these models have been used to study aspects such as the effects of enhanced soft X-rays solar flux over the ionosphere [*Fox*, 2004], the morphology of the ionosphere in the regions close to the terminators [*Fox and Yeager*, 2006], the variability with the 11 year solar cycle [*Krasnopolsky*, 2002], or the effects of solar flares [*Lollo et al.*, 2012]. The only 3-D Martian ionospheric model up to now is the Mars Thermospheric general circulation model (MTGCM) developed at Michigan University [e.g., *Bougher et al.*, 1999], which considers O_2^+, O^+, CO_2^+, and NO^+ below 180 km. The ion-neutral chemistry is taken from *Fox and Sung* [2001], and no plasma transport is included. The MTGCM is a purely thermospheric model that is coupled to the NASA Ames Mars GCM [*Haberle et al.*, 1999] to link the MTGCM to the lower atmosphere. The longitudinal variability of the main peak altitude and electron density predicted by the MTGCM is in agreement with that inferred from MGS measurements [*Bougher et al.*, 2001], showing the importance of the coupling between the neutral atmosphere and the ionosphere [*Bougher et al.*, 2004]. To avoid the problems of linking two different computational codes, a new whole atmosphere model, the Mars Global Ionosphere-Thermosphere Model (M-GITM) is being developed, based on the terrestrial model GITM and for which the physical formulations are based on those on the MTGCM and the NASA Ames GCM [*Bougher et al.*, 2011].

[5] In this paper we will use a ground-to-exosphere Mars GCM, extended to take into account the ionospheric chemistry, to study the variability of the simulated electron density at the peak and its altitude with different atmospheric parameters, and to compare with available observations and previous models.

2. Ionospheric Laboratoire de Météorologie Dynamique Mars GCM

[6] We will use in this study the general circulation model for the Martian ionosphere developed at the Laboratoire de Météorologie Dynamique, the LMD-MGCM. This model, adapted from a terrestrial GCM, has been described elsewhere [*Forget et al.*, 1999] and has been extended to the thermosphere by adding the physical processes relevant in this atmospheric region [*Angelats i Coll et al.*, 2005; *González-Galindo et al.*, 2005, 2009], becoming a ground-to-exosphere model. This allows a self-consistent study of all the atmospheric layers from the surface up to the thermosphere, so that the effects of processes affecting the lower atmosphere are naturally felt in the upper atmosphere, and vice versa.

[7] The model has four significant differences with respect to the model described in *González-Galindo et al.* [2009]. First, the extension of the chemical model used to describe the upper atmosphere [*González-Galindo et al.*, 2005] to include nitrogen chemistry and ionospheric chemistry. Second, a new method to take into account the observed day-to-day variability of the UV solar flux has been implemented. Third, an improved parameterization of the 15 μm CO_2 cooling under Non-Local Thermodynamic Equilibrium (NLTE) conditions has been included. And fourth, the molecular diffusion scheme has been improved. We describe below these improvements, although the last two ones will be described in more detail in forthcoming papers.

2.1. Extended Photochemical Scheme

[8] While the numerical scheme used to compute the changes in the concentrations of the species due to the photochemistry is the same as in *González-Galindo et al.* [2005], the chemical model has been extended and includes now 92 reactions between 25 chemical species. The list of the chemical reactions included in this version of the model can be seen in Tables 1 (for the neutral reactions) and 2 (for the ionospheric reactions). All the photodissociation and photoionization coefficients are calculated by the model, following the scheme described in *González-Galindo et al.* [2005]. The neutral chemical reaction rates are taken from the latest Jet Propulsion Laboratory compilation [*Sander et al.*, 2011], with the following exceptions: the rate for reaction N10 is taken from *Tsang and Hampson* [1986], that for

Table 1. Neutral Chemical Reactions Included in the Model

Number	Reaction
N1	$CO_2 + h\nu \rightarrow CO + O$
N16	$CO_2 + h\nu \rightarrow CO + O(^1D)$
N2	$H + O_2 + CO_2 \rightarrow HO_2 + CO_2$
N3	$O + HO_2 \rightarrow OH + O_2$
N4	$CO + OH \rightarrow CO_2 + H$
N5	$HO_2 + HO_2 \rightarrow H_2O_2 + O_2$
N6	$H_2O_2 + h\nu \rightarrow OH + OH$
N7	$OH + HO_2 \rightarrow O_2 + H$
N8	$H_2O + h\nu \rightarrow H + OH$
N9	$O(^1D) + H_2O \rightarrow OH + OH$
N10	$O + O + CO_2 \rightarrow O_2 + CO_2$
N11	$O + OH \rightarrow O_2 + H$
N12	$O_2 + h\nu \rightarrow O + O$
N17	$O_2 + h\nu \rightarrow O + O(^1D)$
N13	$H + HO_2 \rightarrow H_2 + O_2$
N14	$O(^1D) + H_2 \rightarrow H + OH$
N15	$OH + HO_2 \rightarrow H + H_2O$
N18	$OH + H_2O_2 \rightarrow H_2O + HO_2$
N19	$O(^1D) + CO_2 \rightarrow O + CO_2$
N20	$O(^1D) + O_2 \rightarrow O + O_2$
N21	$O + O_2 + CO_2 \rightarrow O_3 + CO_2$
N22	$O_3 + H \rightarrow OH + O_2$
N23	$O_3 + OH \rightarrow HO_2 + O_2$
N24	$O_3 + HO_2 \rightarrow OH + O_2 + O_2$
N25	$O_3 + h\nu \rightarrow O_2 + O$
N26	$O_3 + h\nu \rightarrow O_2 + O(^1D)$
N27	$H_2 + h\nu \rightarrow H + H$
N28	$N_2 + h\nu \rightarrow N + N(^2D)$
N29	$NO + h\nu \rightarrow N + O$
N30	$N + NO \rightarrow N_2 + O$
N31	$N_2 + O(^1D) \rightarrow N_2 + O$
N32	$N + O_2 \rightarrow NO + O$
N33	$N + OH \rightarrow NO + H$
N34	$N + O_3 \rightarrow NO + O_2$
N35	$N + HO_2 \rightarrow NO + OH$
N36	$N(^2D) + O \rightarrow N + O$
N37	$N(^2D) + N_2 \rightarrow N + N_2$
N38	$N(^2D) + CO_2 \rightarrow NO + CO$
N39	$NO + HO_2 \rightarrow NO_2 + OH$
N40	$O + NO + CO_2 \rightarrow NO_2 + CO_2$
N41	$O + NO_2 \rightarrow NO + O_2$
N42	$NO + O_3 \rightarrow NO_2 + O_2$
N43	$H + NO_2 \rightarrow NO + OH$
N44	$NO_2 + h\nu \rightarrow NO + O$
N45	$N + O \rightarrow NO$

N33 from *Atkinson et al.* [1989], that for N35 from *Brune et al.* [1983], those for N36, N37, and N38 from *Herron* [1999], and that for N45 from *Du and Dalgarno* [1990]. For the ionospheric reactions, the rates used correspond to the values recommended by the 2012 edition of the University of Manchester Institute of Science and Technology Database for Astrochemistry astrochemistry.net [*McElroy et al.*, 2013], with the exceptions of reactions I1, I3, I17, I19, I20, I21, I22, I23, I26, and I27, where we use the same rate as in *Fox and Sung* [2001], and I47 where we use the same value as in *Krasnopolsky* [2002]. The atmosphere is forced to remain globally neutral, so that the electron concentration is equal to the sum of the concentrations of the different ions. Note that the photochemical scheme described here is only used within the GCM in the upper atmosphere (pressures lower than 1 Pa in the simulations shown here). At lower altitudes the GCM employs the scheme described in *Lefèvre et al.* [2004], more appropriate for the study of the Martian lower atmosphere. This should have no effect over the ionosphere, situated at layers well above the transition between both chemical schemes.

[9] The electronic temperature T_e is an important parameter that affects most ionospheric reaction rates. Currently, measurements of T_e limit to those from the retarding potential analyzers (RPA) on the Viking Landers, so we have no hint of the geographical and temporal variability of this parameter. In addition, the RPA measurements of T_e limit to altitudes above about 200 km [*Hanson and Mantas*, 1988], so for lower altitudes uncertain empirical models need to be used. Here we are using a vertical profile of T_e similar to that in Figure 12 of *Barth et al.* [1992], based on Viking measurements [*Hanson and Mantas*, 1988] and calculations of *Rohrbaugh et al.* [1979].

[10] The ionization caused by energetic photochemically produced electrons is included in the model following a parameterization by *Nicholson et al.* [2009]. This secondary ionization has been shown [e.g., *Fox et al.*, 1996] to be important for the correct simulation of the secondary electronic peak.

Table 2. Ionospheric Chemical Reactions Included in the Model

I1	$CO_2^+ + O_2 \rightarrow O_2^+ + CO_2$
I2	$CO_2^+ + O \rightarrow O^+ + CO_2$
I3	$CO_2^+ + O \rightarrow O_2^+ + CO$
I4	$O_2^+ + e^- \rightarrow O + O$
I5	$O^+ + CO_2 \rightarrow O_2^+ + CO$
I6	$CO_2 + h\nu \rightarrow CO_2^+ + e^-$
I7	$CO_2 + h\nu \rightarrow O^+ + CO + e^-$
I8	$CO_2 + h\nu \rightarrow CO^+ + O + e^-$
I9	$CO_2 + h\nu \rightarrow C^+ + O_2 + e^-$
I10	$CO_2^+ + e^- \rightarrow CO + O$
I11	$CO^+ + CO_2 \rightarrow CO_2^+ + CO$
I12	$CO^+ + O \rightarrow O^+ + CO$
I13	$C^+ + CO_2 \rightarrow CO^+ + CO$
I14	$O_2 + h\nu \rightarrow O_2^+ + e^-$
I15	$O + h\nu \rightarrow O^+ + e^-$
I16	$CO_2^+ + NO \rightarrow NO^+ + CO_2$
I17	$CO_2^+ + N \rightarrow CO^+ + NO$
I18	$O_2^+ + NO \rightarrow NO^+ + O_2$
I19	$O_2^+ + N_2 \rightarrow NO^+ + NO$
I20	$O_2^+ + N \rightarrow NO^+ + O$
I21	$O^+ + N_2 \rightarrow NO^+ + N$
I22	$N_2^+ + CO_2 \rightarrow CO_2^+ + N_2$
I23	$N_2^+ + O \rightarrow NO^+ + N$
I24	$N_2^+ + CO \rightarrow N_2 + CO^+$
I25	$N_2^+ + e^- \rightarrow N + N$
I26	$N_2^+ + O \rightarrow O^+ + N_2$
I27	$CO^+ + H \rightarrow H^+ + CO$
I28	$O^+ + H \rightarrow H^+ + O$
I29	$NO^+ + e^- \rightarrow N + O$
I30	$H^+ + O \rightarrow O^+ + H$
I31	$CO + h\nu \rightarrow CO^+ + e^-$
I32	$CO + h\nu \rightarrow C^+ + O + e^-$
I33	$CO + h\nu \rightarrow O^+ + C + e^-$
I34	$NO + h\nu \rightarrow NO^+ + e^-$
I35	$N_2 + h\nu \rightarrow N_2^+ + e^-$
I36	$N_2 + h\nu \; N^+ + N + e^-$
I37	$H + h\nu \rightarrow H^+ + e^-$
I38	$N + h\nu \rightarrow N^+ + e^-$
I39	$N^+ + CO_2 \rightarrow CO_2^+ + e^-$
I40	$N + e^- \rightarrow N^+ + e^- + e^-$
I41	$N_2 + e^- \rightarrow N_2^+ + e^- + e^-$
I42	$O + e^- \rightarrow O^+ + e^- + e^-$
I43	$CO + e^- \rightarrow CO^+ + e^- + e^-$
I44	$CO_2 + e^- \rightarrow CO_2^+ + e^- + e^-$
I45	$O_2 + e^- \rightarrow O_2^+ + e^-$
I46	$CO_2^+ + H_2 \rightarrow HCO_2^+ + H$
I47	$HCO_2^+ + e^- \rightarrow H + CO_2$

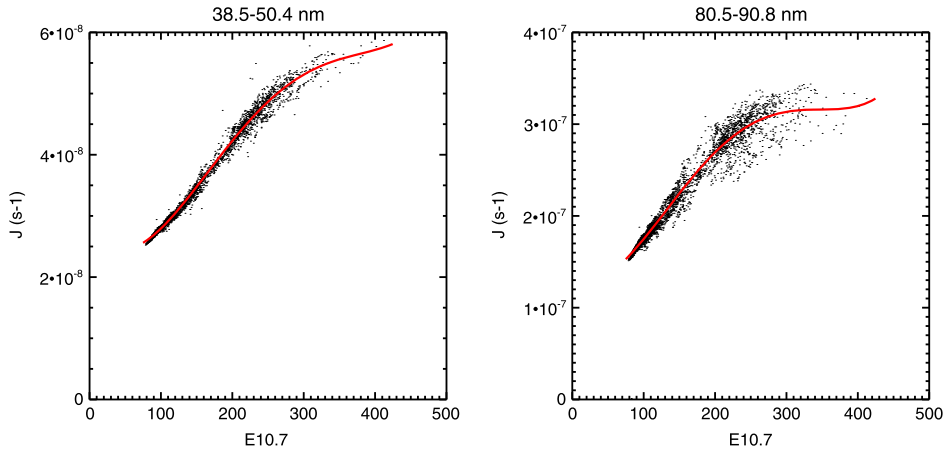

Figure 1. Black dots are the CO_2 photoabsorption coefficient integrated between 38.5 and 50.4 nm (left) and between 80.5 and 90.8 nm (right) (intervals 7 and 16 in Table 1 of *González-Galindo et al.* [2005]) using the daily averaged values of the solar flux for every day between 1976 and 2012, as a function of the E10.7 proxy index. Red line is the polynomial fit of order 5.

[11] The ions, as the neutral species, are transported by the winds, so that their horizontal velocities are determined by the intensity of the general circulation. This ionospheric model is appropriate to the study of the photochemical region of the ionosphere, below about 180 km. Above this altitude, plasma dynamics processes, as well as the interaction with magnetic fields, not included in the model, become important, so the results of the model are not reliable above that altitude. The effects of precipitating electrons are neither included in the model. A companion paper (J.-Y. Chaufray et al., submitted to Journal of Geophysical Research, 2013) describes the work intended to include the plasma dynamics into the model and thus to extend its validity above 200 km.

2.2. Implementation of a Daily Variable Solar Flux

[12] *González-Galindo et al.* [2005] described a strategy to incorporate fast calculations of photoabsorption coefficients and UV heating rates in the LMD-MGCM, including a sinusoidal adjustment to take into account the solar cycle variability. The sinusoidal fit, although valid to incorporate to a first order the 11 year solar variability, was not appropriate to incorporate shorter scale variability. Our objective here was to extend the procedure described in *González–Galindo et al.* [2005] to take into account the day-to-day variability of the solar flux.

[13] The first step was to obtain daily values of the solar flux, with the appropriate spectral coverage (0.1–800 nm), at least from the arrival of MGS to Mars up to the present. For this purpose we have used the Solar Irradiance Platform [*Tobiska and Bouwer*, 2006] (SIP, version 2.37 for this study) to obtain daily averaged values of the solar flux in the desired spectral interval for every day between 1976 up to 2012 (more than three solar cycles). The solar flux was then rescaled to the average Sun-Mars distance.

[14] Second, using the daily averaged solar fluxes obtained in the previous step, the photoabsorption coefficients at the top of atmosphere for each considered species i and spectrally integrated in each of the spectral subintervals k in Table 1 of *González-Galindo et al.* [2005], $j_{i,k}^{\mathrm{TOA}}$, were calculated for each day by

$$j_{i,k}^{\mathrm{TOA}} = \int_{\lambda 0}^{\lambda 1} F_{\mathrm{TOA}}(\lambda)\sigma_i(\lambda)\mathrm{d}\lambda \qquad (1)$$

where $\lambda 0$ and $\lambda 1$ are the limits of the spectral subinterval considered, $F_{\mathrm{TOA}}(\lambda)$ the solar flux at the top of the atmosphere and $\sigma_i(\lambda)$ the photoabsorption cross section of the species i. For this purpose, we used a detailed 1-D model [*López-Valverde et al.*, 2006; *González–Galindo*, 2006] (considering only the variation with altitude), updated with the most recent measurements of the photoabsorption cross sections of the different molecules obtained from the MPI-Mainz-UV-VIS spectral atlas of gaseous molecules (Keller-Rudek, H. and G. K. Moortgat, MPI-Mainz-UV-VIS Spectral Atlas of Gaseous Molecules, www.atmosphere.mpg.de/spectral-atlas-mainz).

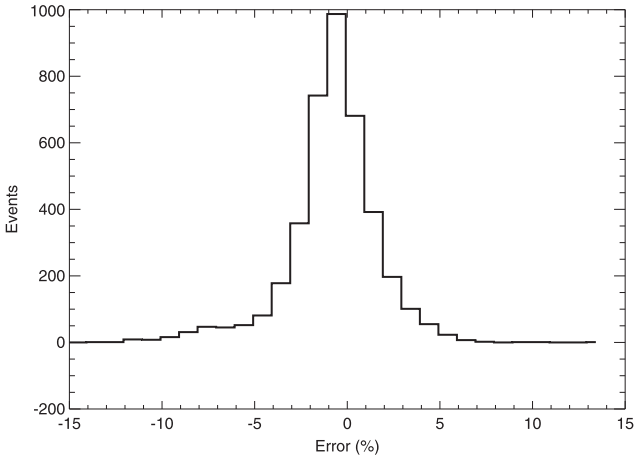

Figure 2. Histogram of the differences (in percentage) between the total CO_2 photoabsorption coefficient calculated using a detailed spectral integration and that calculated using the fit to the E10.7 values.

[15] And third, for each of the spectral subintervals, the integrated photoabsorption coefficient of each species calculated for each of the days was plotted as a function of the daily value of the E10.7 proxy parameter, and a polynomial fit of order 5 applied (see two examples in Fig. 1).

[16] So to calculate the total photoabsorption coefficients (from which the UV heating rate, as well as photodissociation and photoionization rates can be derived) of the different species for a given day, one only needs to know the value of the proxy index E10.7 for that day (it can be obtained from the SIP), calculate the photoabsorption coefficients at top of atmosphere integrated in each of the spectral subintervals using the polynomial fits, and sum over all the spectral subintervals. The variation with altitude of the photoabsorption coefficients is then calculated using the same procedure as in *González-Galindo et al.* [2005]. This method is much faster (around a factor of 100) than the detailed spectral integration.

[17] To check the quality of this procedure, we have calculated for each day between 1986 and 1998 (corresponding approximately to the duration of solar cycle 22) the total photoabsorption coefficients for each species using two methods: first, a rigorous spectral integration and second the proposed fit to the daily values of the E10.7 proxy index. The difference between the two coefficients obtained with each method at the top of atmosphere is then calculated for each day. Figure 2 shows the histogram of these differences for CO_2. It can be seen that most of the time the difference is lower than 5%, the standard deviation of a fitted Gaussian is of about 1.5%, and the systematic error is smaller than 1%. The differences remain at similar levels (generally lower than 5%) at all altitudes. The only exception is the first spectral subinterval (the one representing the most energetic radiation, between 0.1 and 5 nm) at altitudes below about 100 km, where the differences can be as high as 40–50%. This is due to the strong spectral variability of the CO_2 photoabsorption cross section between 0.1 and 5 nm, which can not be correctly represented by just one spectral interval, and is one of the aspects of the model that needs to be improved in the future. On behalf of this, we can conclude that the proposed procedure produces photoabsorption coefficients with a good degree of precision and with a considerable saving of CPU time.

[18] It has to be taken into account that this procedure uses solar fluxes measured at Earth and applies them directly to Mars, without correcting for the Sun-Earth-Mars angle. This can introduce a nonnegligible error when applying this method to a given day [*Forbes et al.*, 2006]. However, for comparisons with large data sets spanning long periods, such as the ones presented in this paper, the average error should be small.

2.3. Improved 15 μm Cooling Parameterization

[19] Previous studies [*Forget et al.*, 2009; *González–Galindo et al.*, 2009] have shown that the mesopause simulated by the LMD-MGCM was too high and too warm when compared with observations. These studies identified the parameterization of the cooling due to CO_2 15 μm emissions under NLTE as the likely responsible. That parameterization, based on previous calculations with a detailed 1-D model [*López-Puertas and López-Valverde*, 1995] included a number of simplifications that affected the radiative transfer and made use of a fixed, constant, and uniform atomic oxygen concentration, instead of the variable atomic oxygen profile calculated by the GCM (see *Forget et al.* [2009] and *González-Galindo et al.* [2009] for more details).

[20] An improved parameterization of this physical process, essential for the thermal balance of the mesosphere and thermosphere of Mars, has been developed recently to overcome those limitations [*López-Valverde et al.*, 2011]. Here we will only sketch the main features of this parameterization, as a detailed description of the scheme and its effects on the simulated temperatures will be published elsewhere.

[21] Regarding the radiative transfer, the number of molecular levels and the transitions between them has been increased: instead of using two "virtual" molecular levels, five "real" CO_2 levels and bands are taken into account. Also the cool-to-space approximation has been substituted by a calculation of the full exchange between atmospheric layers. Another important improvement of this parameterization is that the actual atomic oxygen profile calculated by the model (spatially and temporally variable, following the simulated photochemistry, vertical diffusion, and horizontal transport by the general circulation) is taken into account. As a result of all these improvements, temperatures simulated by the model in the upper mesosphere/lower thermosphere region are in much better agreement with the Spectroscopy for Investigation of Characteristics of the Atmosphere of Mars (SPICAM) observations [*López-Valverde et al.*, 2011; *González-Galindo et al.*, 2011].

2.4. Improved Molecular Diffusion Scheme

[22] The vertical velocity of each species is the sum of the momentum-weighted mean vertical velocity w_m plus the diffusion velocity w_i or deviation of vertical velocity of the ith species from mean velocity [*Dickinson and Ridley*, 1972]. This diffusion velocity coupled to the continuity equation leads to the molecular diffusion equation. The densities of atomic and molecular hydrogen were not well described in the previous version of the LMD-MGCM. We have developed a new algorithm to solve the molecular diffusion equation [*Chaufray et al.*, 2012] that describes better the behavior of these chemical species. In this algorithm, the diffusion velocity of each species is assumed to be independent of the other species' diffusion velocity. The molecular diffusion is solved on an altitude grid rather than the usual hybrid vertical coordinate used in the GCM (terrain following in the lower atmosphere and nearly pressure in upper atmosphere). The choice of the altitude rather than pressure level is due to the pressure variation due to diffusion implying that, in pressure coordinates, any temporal variation must be corrected by a term taking into account the pressure variation at a given altitude. For each species, the lower boundary condition at z_0 is a constant mass density $\rho_i(t + \mathrm{d}t, z_0) = \rho_i(t, z_0)$. The upper boundary condition is the diffusive equilibrium for each species except H and H_2; for these we assumed that the vertical velocity is the effusion velocity (Jeans escape). Discretization of the diffusion equation led to the inversion of a tridiagonal matrix, which was performed using the Thomas algorithm. This procedure was used in the 1-D upper atmosphere model developed at the Instituto de Astrofísica de Andalucía (IAA) [*González-Galindo*, 2006] and is described for example in the appendix O of *Schunk and Nagy* [2009].

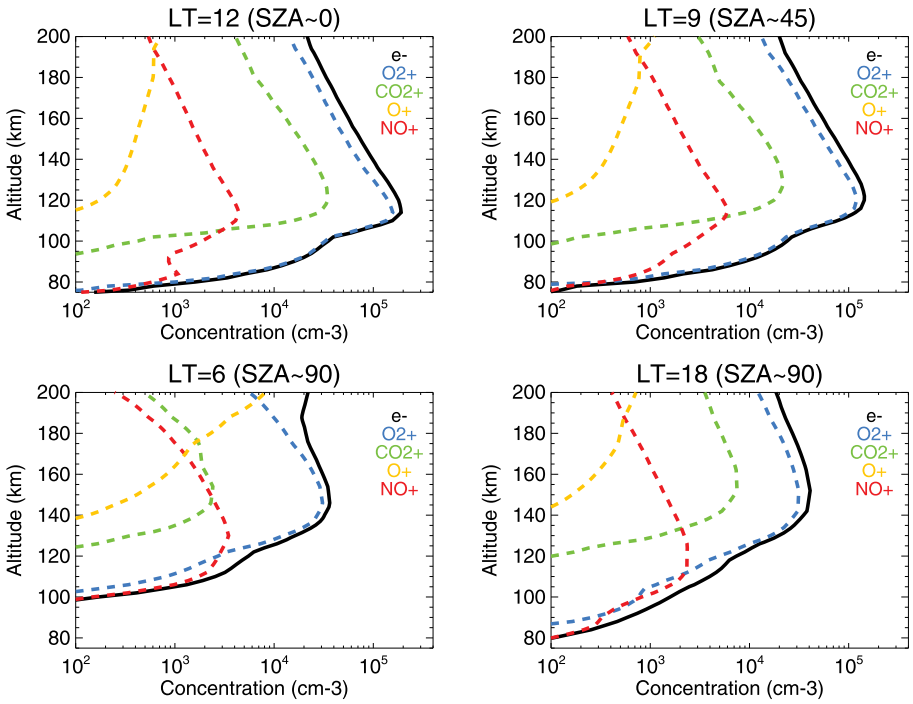

Figure 3. Electron (solid black lines), O_2^+ (dashed blue lines), NO^+ (dashed red lines), CO_2^+ (dashed green lines), and O^+ (dashed orange lines) profiles obtained at LT = 12, 9, 6, and 18 at lat = 0, lon = 0 (corresponding approximately to SZA = 0, 45, 90 and 90, respectively). The profiles are time averages for the L_s = 0–30 period.

2.5. Simulations Used in This Work

[23] Diverse GCM simulations were performed for this study. First, as a reference, a simulation for a full Martian year using the dust load as observed by MGS during MY27 and a constant solar flux appropriate for solar average conditions (as in *González-Galindo et al.* [2009]) was performed. A second simulation included the measured day-to-day variability of the UV solar flux during MY27 and was used to study the effects of the solar variability. Finally, in order to compare with MGS measurements spanning different periods of MY24, MY25, MY26, and MY27, simulations including the appropriate dust load and daily variable solar

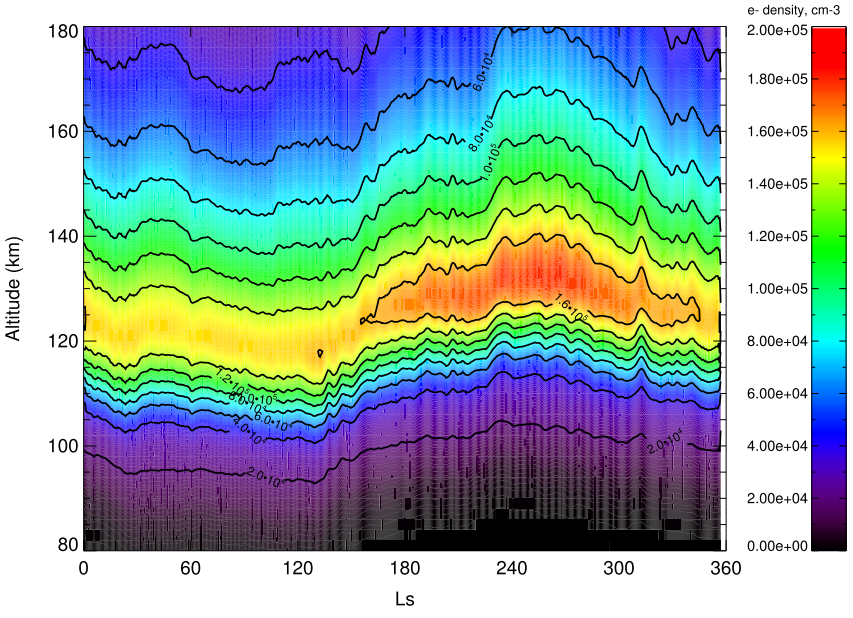

Figure 4. Variation of the electron density at the subsolar point during a full Martian year as a function of altitude and time, when using a constant solar flux appropriate for solar average conditions.

flux for each of the MGS ionospheric observation periods have also been performed.

[24] All the simulations have been made on a 64 (longitude) × 48 (latitude) × 49 (vertical) grid, giving a horizontal (lon-lat) resolution of 5.625° × 3.75°. The vertical grid is not regular, with higher resolution close to the surface. The vertical resolution in the upper atmosphere is of around 7 km.

3. Results

[25] Figure3 shows electronic and ionic profiles predicted by the model for the simulation with the constant solar flux. They are time-averaged profiles for the L_s=0–30 period and are obtained at different local times at the point with latitude 0 and longitude 0; these results can be considered as typical profiles.

[26] The shape of the electronic profile is similar to those measured by MGS and MaRS. The profiles show a well defined primary peak, while the secondary peak is not very neat and looks more like a shoulder rather than like a peak. In fact, as we will show later (section 4), comparisons with MGS profiles show that the simulated secondary peak is significantly less important that the observed one. Previous works [*Bougher et al.*, 2001; *Fox*, 2004] have shown the importance of the solar X-ray fluxes to simulate a significant secondary peak. Our scheme to calculate the photoabsorption and photoionization coefficients groups in only one spectral subinterval all the wavelengths between 0.1 and 5.0 nm. This is probably a too crude representation, as the CO_2 photoabsorption cross section is highly variable in this spectral range, and underestimates the contribution of the shortest wavelengths. As shown in section 2.2, the differences between the photoabsorption coefficient integrated in this spectral subinterval calculated by a detailed spectral integration and by the procedure used in the LMD-MGCM can get to 50% at altitudes typical of the secondary peak. This aspect needs to be improved in a future version of the model.

[27] For the noon case, the electron density at the peak is of about $2 \cdot 10^5$ cm^{-3} and the altitude of the peak is close to 120 km. This is in agreement with the properties of the peak measured by MGS [*Fox and Yeager*, 2009] and MARSIS [*Nielsen et al.*, 2006; *Morgan et al.*, 2008]. A more detailed comparison with available measurements will be presented in section 4. For the LT = 9 case, the profile is very similar to the noon case, showing a weak variation with SZA, when this is lower than about 45°. When going to higher values of SZA, the concentration of the peak strongly decreases and its altitude increases. So at dawn and dusk the peak concentration is about one third that at noon, and the altitude of the peak is of about 140–150 km.

[28] In agreement with observations, the Martian ionosphere below about 200 km is dominated by O_2^+. CO_2^+ is the second most abundant ion above about 100 km and NO^+ below. O^+ increases its relative abundance in high layers. Note also the asymmetry between morning and evening sides, in particular concerning the relative abundance of the different ions. CO_2^+ is more abundant in the evening side, while O^+ is more important in the morning side, where it becomes the dominant ion above 200 km. Above about 180 km, these results may be affected by plasma dynamics, as mentioned above. According to (J.-Y. Chaufray et al., submitted manuscript, 2013), the peak of O^+ density is moved downwards when plasma transport is considered, while the concentrations of O_2^+ and CO_2^+ are only slightly affected by transport. However, the overall behavior described before, including the morning-evening asymmetry, is not modified by the inclusion of the plasma dynamics (J.-Y. Chaufray et al., submitted manuscript, 2013).

[29] This morning-evening asymmetry in the ionospheric composition is related to a similar asymmetry in the temperature structure and in the distribution of the neutral species. The temperature is higher in the evening terminator than in the morning terminator [see *González-Galindo et al.*, 2009, Figure 3], inducing differences in the scale height and in the vertical distribution of the different species. So for this particular case, atomic oxygen becomes as abundant as CO_2 at about 200 km for LT = 18 and at about 160 km for LT = 6. The higher relative abundance of atomic oxygen around the morning terminator explains the higher abundance of O^+ at LT = 6. This result is another demonstration of the importance of using a 3-D self-consistent model able to take into account the feedbacks between dynamics, thermal structure, and composition. There are observational evidences of asymmetries between the morning and the evening terminator. *Safaeinili et al.* [2007] analyzed MARSIS Total Electron Content data and found that the scale height was higher during sunset than during sunrise (indicating higher temperatures, in agreement with the results of the model) and that the peak electron density was on average 50% higher at sunset than at sunrise. The model does not predict such an asymmetry in the peak electron density between the morning and evening terminator in this particular case. However, it has to be taken into account that the results shown in Figure 3 are temporally averaged results for the L_s=0–30 season.

[30] In the rest of this section we will focus on the primary ionospheric peak and in particular on the different factors that produce its variability.

3.1. Seasonal Variation of the Subsolar Main Ionospheric Peak

[31] We focus here on studying the seasonal variability of the altitude and electron density of the main electronic peak for low SZA. Figure 4 shows the variability during a full Martian year of the electronic profile at the subsolar point, for the simulation with a constant solar flux. Let us remind that the perihelion occurs at L_s = 250° (L_s = 270° corresponding to the Southern summer solstice) and aphelion at L_s = 70° (L_s = 90° the Northern summer solstice), while the equinoxes are at L_s = 0° and L_s = 180°.

[32] Both the electron density at the primary peak and its altitude vary during the Martian year. The electron density is minimum (about $1.52 \cdot 10^5$ cm^{-3}) during the aphelion season (at L_s = 90) and maximum (around $1.77 \cdot 10^5$ cm^{-3}) before the perihelion season (at L_s = 255). This variation between aphelion and perihelion reflects the dependence of the peak electron density with the solar flux: at perihelion more photons arrive at the top of the Martian ionosphere, producing an enhanced ionization and thus more electrons. Note that the ratio of electron density at perihelion and aphelion (about 1.16) is similar to the inverse ratio of the corresponding heliocentric distances (about 1.20). That is, to a first order

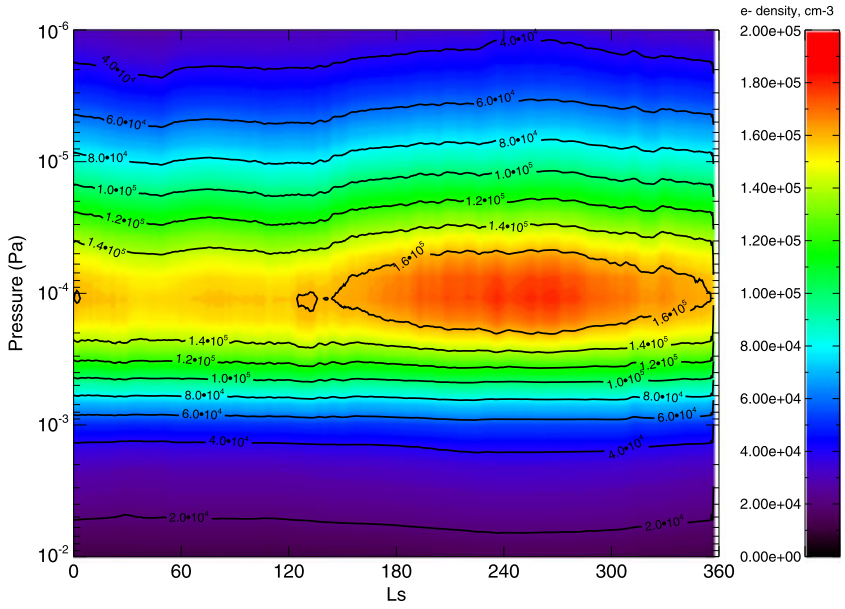

Figure 5. Variation of the electron density at the subsolar point during a full Martian year as a function of atmospheric pressure and time, when using a constant solar flux appropriate for solar average conditions.

the peak electron density is proportional to the inverse of the heliocentric distance, as would be expected from a simple ionospheric model [*Mendillo et al.*, 2003]. Also the altitude of the electronic peak is minimum (118 km) around L_s = 90 and maximum (134 km) around L_s = 250. The altitude is about 126 km in both equinoxes, i.e., the seasonal variation is approximately a harmonic oscillation with an amplitude of 8 km around the equinox/mean peak altitude. This seasonal variation of the altitude of the peak electron density is in good agreement with the $\approx$ 15 km variation between aphelion and perihelion found with the MTGCM [*Bougher et al.*, 2000].

[33] Is this altitude variation also a direct effect of the variation of the solar flux reaching the top of the Martian atmosphere due to the orbital eccentricity of the planet? Figure 5 is similar to Figure 4 except that the electronic profiles are represented as a function of pressure, and not of altitude. Clearly, the ionospheric peak is placed at approximately the same pressure level during the full Martian year, as expected for a constant solar flux. This implies that the altitude variation of the electronic peak is linked to the altitude variation of constant pressure levels in the atmosphere. That is, the inflation/contraction of the atmosphere, driven by the seasonal variation of the temperatures in the lower

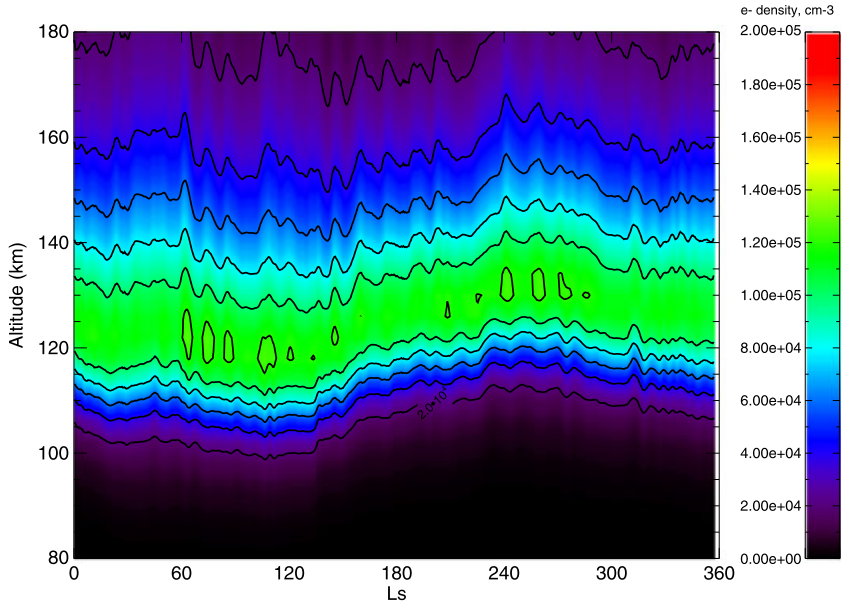

Figure 6. Variation of the electron density at the subsolar point during a full Martian year as a function of altitude and time, when using a daily variation of the solar flux as observed during MY27.

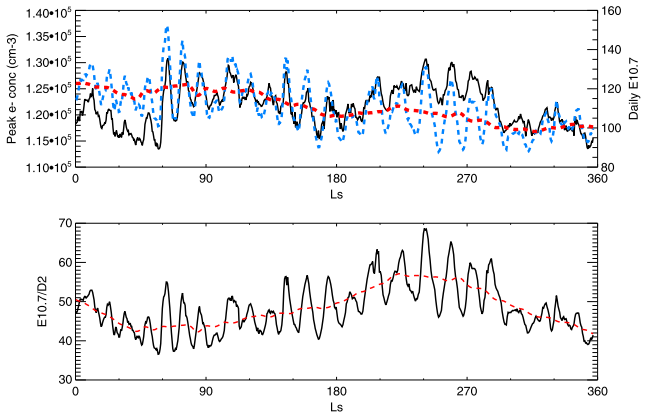

Figure 7. (top) Peak electron density at the subsolar point as simulated for MY27 (black solid line), proxy index E10.7 for this Martian year (blue dashed line), and smoothed E10.7 to emphasize the seasonal evolution (red dashed line). (bottom) Daily value of E10.7 index divided by the square of the Sun-Mars distance (black solid line) and smoothed value of E10.7 divided by the square of the Sun-Mars distance (red dashed line).

atmosphere, is at the origin of the altitude variation of the electronic peak. This is in agreement with recent analysis of MGS ionospheric observations, which show that the altitude of the peak is mainly driven by the neutral effective scale height between about 20 km above the surface and the altitude of the peak [*Zou et al.*, 2011], and also with previous modeling results [*Bougher et al.*, 2001].

[34] The previous results were obtained using a constant solar flux through all the simulated Martian years. However, during a "real" Martian year the solar flux is subject to variability, combining long-term variability due to the 11 year solar cycle and short-term variability due to the solar rotation or other factors. To check the effects of this variability, we show in Figure 6 a plot similar to Figure 4 but for the simulation using a variable solar flux as observed for MY27.

[35] For this simulation, the simulated electron density is smaller than for the simulation with the constant solar flux. This is expected, as the constant solar flux used in the simulation was appropriate for solar average conditions, while during MY27 the Sun was at a minimum of its activity cycle. The maximum electron density predicted by the model decreases from about $1.77 \cdot 10^5$ cm^{-3} for the constant solar average flux to about $1.27 \cdot 10^5$ cm^{-3} for the MY27 solar flux. But also the seasonal variability of the peak concentration changes. For the MY27 solar flux simulation, the peak electron density remains almost constant during the whole year, in clear contrast with the variability obtained in the simulation using a constant solar flux. However, the variability of the peak altitude is similar to that simulated for the constant solar flux for solar average conditions.

[36] In order to better understand these results, we show in Figure 7 (top) the peak electron concentration as a function of the day during the simulated MY27, together with the observed variability of the E10.7 solar proxy index during that Martian year.

[37] In general, the solar activity during MY27 is characterized by an overall decrease from the beginning to the end of the year. The solar activity is at its highest between Martian solar days 120 and 200, producing an increase in the peak electron density. During perihelion, the solar activity is significantly lower than at aphelion. This decrease of the solar activity compensates for the planet being closer to the Sun, and the overall result is that the seasonal variability of the peak electron density during MY27 is quite small. In Figure 7 (bottom) we show the daily and the smoothed values of the E10.7 proxy index, corrected for the varying Sun-Mars distance. We can see that, when taking into account the solar variability and the eccentricity of the Martian orbit, there are more available photons during perihelion than during aphelion. However, this does not reflect in a significantly higher peak electron density during perihelion. It has to be taken into account that simple ionospheric models based on Chapman theory show that the expected peak electron density is directly proportional to the square root of the available ionizing solar flux, but also inversely proportional to the square root of the scale height (that is, the temperature) [*Mendillo et al.*, 2003; *Withers and Mendillo*, 2005]. In addition, the variability of the neutral composition can also induce additional departures from a simple Chapman model.

[38] For the altitude of the peak, as it was mentioned before, it is mainly determined by the thermal structure of the lower atmosphere. The temperatures in the lower atmosphere are driven by the solar IR radiation. The main variability of the solar IR radiation reaching Mars' lower atmosphere is that produced by the eccentricity of the orbit, since the solar cycle variation in the IR is minimal. The result is that the seasonal behavior of the peak altitude during MY27 is essentially independent of the UV solar flux.

[39] It is also worth noting that the peaks in the E10.7 variability, due to the 26 day solar cycle, are clearly reflected in the peak concentration obtained with the model. This additional ionospheric variability due to the solar rotation has already been observed [*Withers and Mendillo*, 2005; *Nielsen et al.*, 2006], and the magnitude (about 15–20%) of the simulated variability agrees well with the observed variability.

3.2. Variation With SZA and the Nighttime Ionosphere

[40] As discussed in section 1, the concentration and altitude of the main ionospheric peak have been observed to vary with SZA [e.g., *Fox and Yeager*, 2009]. Figure 8 shows the variability of the modeled ionosphere, during the L_s = 0–30 season, as a function of altitude and local time. The electron density is maximum at noon and around 120 km and does not show a strong variability between LT ≈8–16 (SZA lower than about 60° for this season at the equator). Around the terminators there is a strong decrease of the peak electron density at all altitudes of about 2 orders of magnitude in about 2 h. It can be clearly seen that the model predicts the presence of a nocturnal ionosphere, with electron densities of the order of 100 cm^{-3}. The electron density at night increases with altitude, reaching concentrations close to 1000 cm^{-3} at about 180 km. Below about 160 km the nighttime ionosphere decreases steadily from dusk to dawn. At the very top altitudes the "night" starts after LT = 22, due to the remaining illumination up to SZA ≈ 104°.

[41] What is producing this nightside ionosphere? Given that here we are not considering phenomena such as electron precipitation or plasma transport, which have been

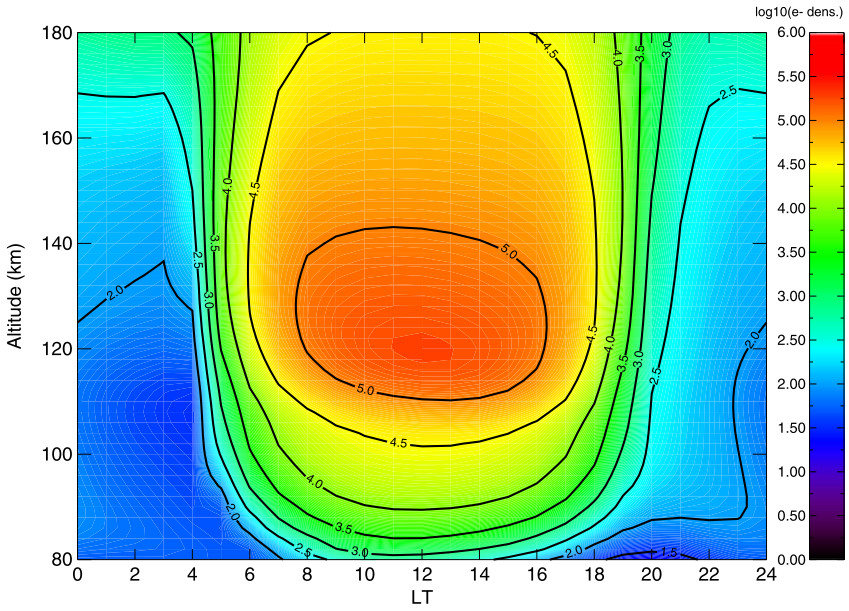

Figure 8. Electron density for the L_s = 0–30 season as a function of altitude and local time, for latitude 0 and longitude 0. A logarithmic color scale is used, so that 5 means 10^5 cm^{-3}.

suggested to be at the origin of the observed nighttime ionosphere, the only answers can be the photochemistry or the general circulation. Tests in which the ions and electrons are not transported by the general circulation have been made, showing almost no difference in the ionospheric behavior. This leaves the photochemistry as the only possible responsible of the simulated nightside ionosphere. Figure 9 shows the composition of the ionosphere at 120 km as a function of local time. At the beginning of the night O_2^+ is lost by electron dissociative recombination (reaction I4 in table 2), but also transformed in NO^+ by reactions I18, I19 and I20, so that NO^+ becomes the dominant ion at this altitude during the night. Given that, in contrast with other ions, NO^+ is only lost by its dissociative recombination I29 (with a rate similar to that of O_2^+ dissociative recombination), but not by other reactions, its lifetime is long (of the order of few hours at the middle of the night) and NO^+ can survive during the night, even in the absence of any production. That is, NO^+ created at a given point during the day can remain for hours, even when the night arrives and the other (faster) ions have already dissapeared. Even the 1-D version of the model (with no winds) predicts the presence of a nightside ionosphere formed by NO^+, showing that the general circulation is not its major driver. At higher altitudes (around 170–180 km), the atmosphere is less dense and the conversion of O_2^+ to NO^+ is less efficient, so at these layers and above O_2^+ is predicted to be the main constituent of the Martian nightside ionosphere. However, the results at these altitudes have to be considered with caution, given that plasma dynamics are likely to modify this behavior. The modification of the modeled nightside ionosphere when including plasma dynamics processes is discussed in (J.-Y. Chaufray et al., submitted manuscript, 2013), who find an increase of O_2^+ and NO^+ densities between 120 and 150 km in the nightside.

[42] Previous studies have addressed the composition of the nightside ionosphere of Mars. *Haider* [1997] found, using a 1-D steady state model including chemistry and electron precipitation, that NO^+ was the dominant component of the nightside ionosphere below about 140 km, with O_2^+ being more abundant in upper layers. In our calculations, NO^+ dominates up to about 170 km. The electron densities predicted in *Haider* [1997] are about one order of magnitude higher than those predicted by our model. Different factors can contribute to these differences: (1) the calculations in *Haider* [1997] include magnetospheric electron precipitation, not included in our model; (2) *Haider* [1997] uses a fixed temperature and fixed neutral atmosphere, and thus the calculations are not completely self-consistent; and (3) the model used in *Haider* [1997] is a 1-D steady state model, not a time-marching model able to describe the temporal variability of the ionosphere in the day-night transition. *Fox et al.* [1993] found that the nightside ionosphere was

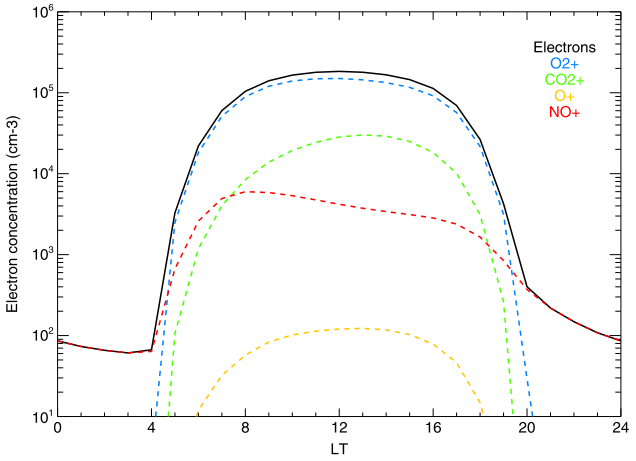

Figure 9. Electron and ion concentration for the L_s = 0–30 season at 120 km, latitude 0 and longitude 0, as a function of local time.

Table 3. Observational Characteristics of MGS Data Subsets

Set Number	Date of Acquisition	Number of Observations	Martian Year	L_s Range	Lat Range	LT Range
1	[1998-12-24, 1998-12-31]	32	24	[74.1, 77.3]	[64.7, 67.2]	[3.4, 4.3]
2	[1999-03-09, 1999-03-27]	43	24	[107.6, 115.9]	[69.7, 73.3]	[3.6, 4.1]
3	[1999-05-06, 1999-05-29]	220	24	[134.7, 146.2]	[-69.1, -64.6]	[12.0, 12.2]
4	[2000-11-01, 2001-01-31]	732	25	[70.2, 110.9]	[63.4, 77.6]	[2.8, 3.1]
5	[2001-02-01, 2001-06-06]	840	25	[110.9, 173.8]	[69.0, 85.5]	[3.1, 8.8]
6	[2002-11-01, 2002-12-31]	526	26	[89.0, 116.3]	[60.6, 73.5]	[3.6, 4.1]
7	[2003-01-01, 2003-03-21]	650	26	[116.6, 155.5]	[73.6, 84.4]	[4.1, 12.3]
8	[2003-03-22, 2003-06-04]	630	26	[155.9, 197.3]	[69.1, 81.0]	[12.4, 14.1]
9	[2003-06-22, 2003-07-02]	76	26	[207.8–214.1]	[68.4, 68.5]	[13.9, 14.1]
10	[2004-11-23, 2004-12-22]	270	27	[119.0, 132.8]	[61.8, 70.1]	[4.4, 5.1]
11	[2004-12-26, 2005-03-31]	877	27	[134.6, 185.2]	[71.1, 80.1]	[5.3, 13.5]
12	[2005-04-01, 2005-06-09]	704	27	[185.3, 227.3]	[64.9, 71.8]	[13.5, 14.7]

dominated by O_2^+, but this work did not consider chemistry, only ion transport and auroral precipitation and only altitudes above 170 km were considered.

[43] How does the nightside ionosphere simulated by our model compare to observations? A review of the existing measurements of the nightside ionosphere can be found in *Withers et al.* [2012b]. All the observations show a patchy, irregular nightside ionosphere that sometimes can reach intensities close to 10^5 cm^{-3}, sometimes are much weaker, of the order of 1000 cm^{-3} for MaRS observations (that can be considered as the detection limit for the instrument), [*Withers et al.*, 2012b], and sometimes are below the detection limit of the instruments. The ionosphere simulated in the deep nightside contains about 100 cm^{-3} electrons at 120 km, which is much weaker than the ionospheric "patches" observed. However, most of the observations of the nightside ionosphere have been made at SZA between about 105 and 120 (that for this season and location corresponds roughly to local times between 19 and 20 at the dusk side). At LT = 19, the model predicts electron densities that can reach levels of about 3–5·10^3 cm^{-3}. This concentration is compatible with some of the MaRS observations [*Withers et al.*, 2012b]. It has also to be remembered that the limit of detection of other instruments studying the ionosphere, such as the Viking radio science instrument or the Mars Express radar is around $5 \cdot 10^3$ cm^{-3} [*Zhang et al.*, 1990; *Gurnett et al.*, 2008; *Withers et al.*, 2012b]. The comparison with the observations suggests that this nighttime photochemical ionosphere simulated by the LMD-MGCM can be a relevant component of the ionosphere around the evening terminator. Around midnight it is just a residual background component on top of which a patchy ionosphere

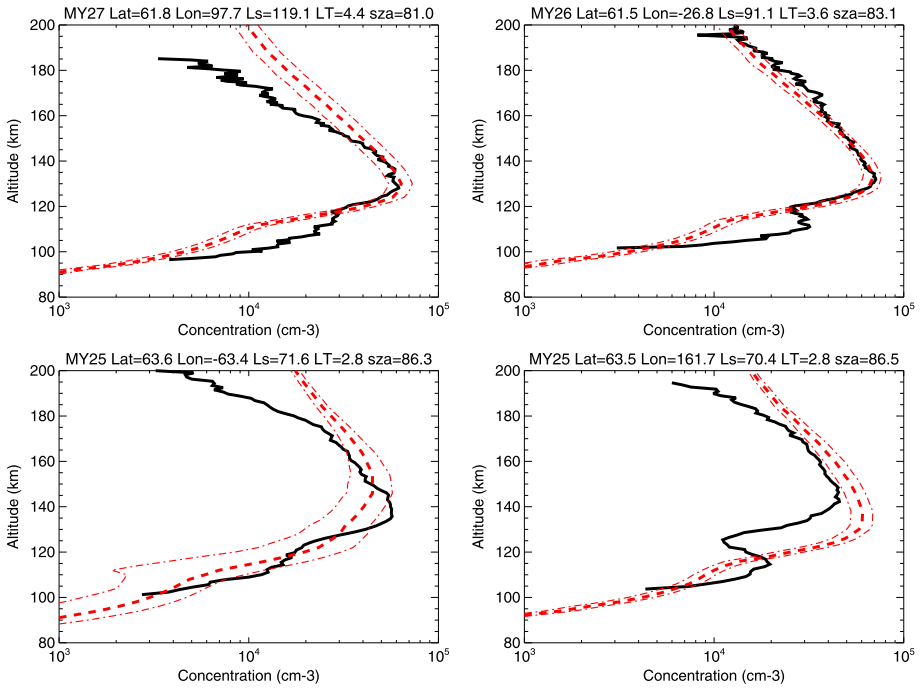

Figure 10. Comparison of four electronic profiles measured by MGS (black solid lines) with the LMD-MGCM predicted profiles interpolated to the same location and time (red dashed lines). The thin red dash-dotted lines represent the temporal and geographical variability in the GCM results (see text). The location of each profile is shown above each panel.

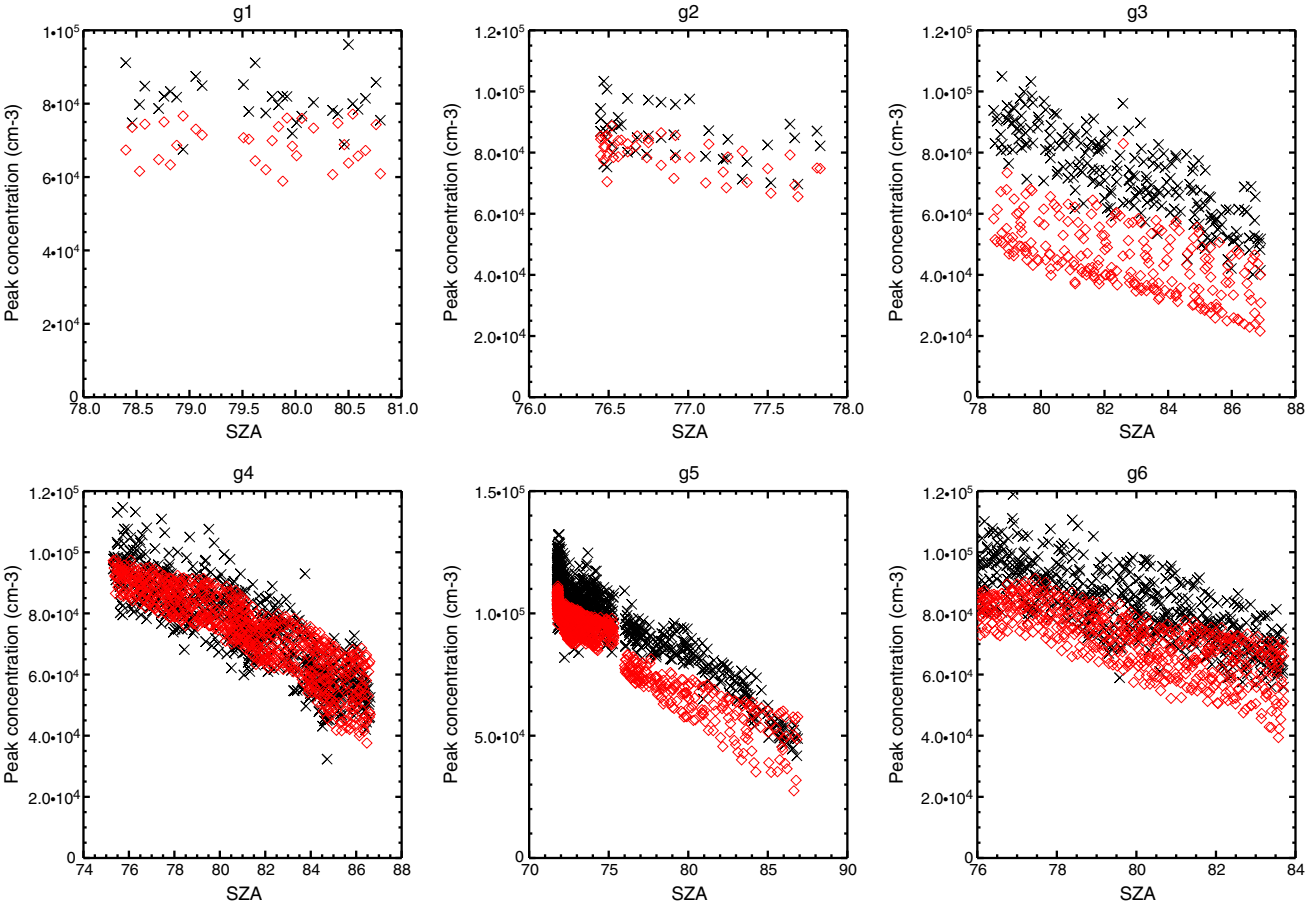

Figure 11. MGS (black crosses) and GCM-simulated (red diamonds) electron density at the main electron peak, as a function of SZA, for the MGS RSS subsets 1–6 described in Table 3.

seems to be present. Other processes, like electron precipitation, must be producing significant local enhancements [*Lillis et al.*, 2011; *Withers et al.*, 2012a]. It has been shown [*Lillis et al.*, 2009] that the location of nightside electron precipitation is controlled by the geometry and topology of the crustal magnetic fields, so that electrons precipitate where fields are predominantly vertical.

4. Comparison With Observations and Previous 3-D Modeling Results

[44] How does the ionospheric variability simulated by the LMD-MGCM and summarized in the previous section compare with the data? We will first compare with the data obtained by MGS Radio Science Subsystem (RSS), which can be divided in 12 subsets as indicated in Table 3. As can be seen, MGS RSS observations span different periods during 4 different MYs. As explained in section 2.5 we have performed simulations using the observed daily variation of the UV solar flux and the observed dust load of the lower atmosphere during these Martian years. For the purpose of comparison, the results of these simulations have been interpolated to the particular geographical and temporal location of each MGS observation. Although not shown in Table 3, each MGS observation or profile spans a lat/lon extension very small compared to our GCM grid. Let us recall that for these simulations we used a GCM lon/lat resolution of $5.625 \times 3.75°$.

[45] We show in Figure 10 four examples of comparisons between observed MGS electronic profiles (black lines) and our simulated profiles (red lines), representative of different but typical situations. In some cases the model correctly predicts the altitude and concentration of the main electronic peak and also the slope of the electronic profile above the peak (top right). In some other cases the peak altitude and concentration are correctly simulated, but not the slope above the peak (top left). And in some others the simulated ionospheric peak is different from the observed one (bottom). It is also evident from Figure 10 that the model systematically underestimates the concentration at the secondary peak, as already mentioned in section 3.

[46] Caution has to be taken in the comparison of a GCM to these data. A GCM with a horizontal grid size of more than 100 km is not the best tool to perform a profile-to-profile comparison: observed profiles can be affected by small-scale processes, such as gravity wave propagation, not included in the GCM [e.g., *Spiga et al.*, 2012]. However, these effects should minimize when extending the comparisons to large data sets, as we do next. Also we added an "error bar" to the GCM calculations in Figure 10. This is

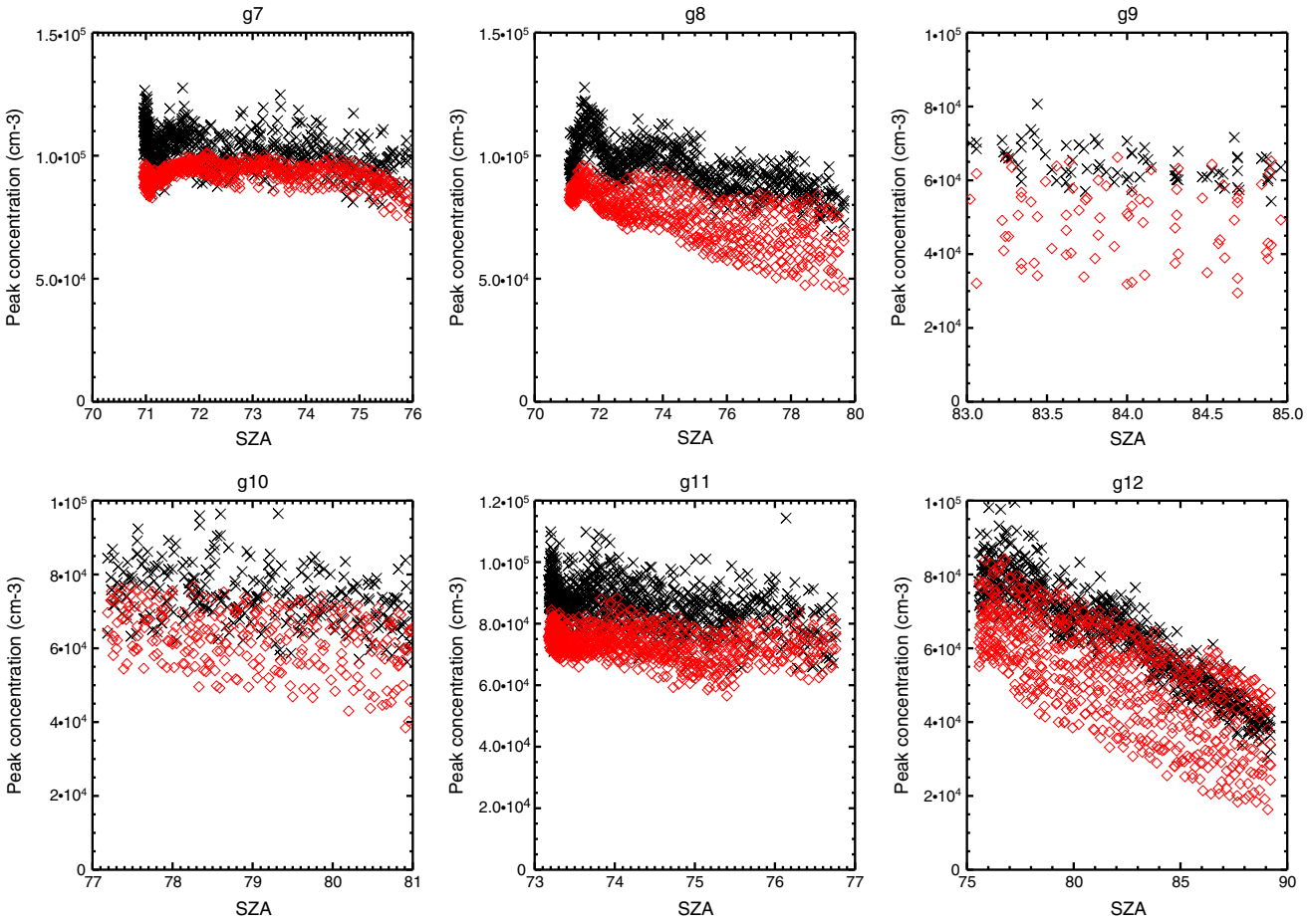

Figure 12. MGS (black crosses) and GCM-simulated (red diamonds) electron density at the main electron peak, as a function of SZA, for the MGS RSS subsets 7–12 described in Table 3.

intended to illustrate one of the largest source of internal variability in the model, which is the temporal and geographical variability around the simulated point. For this purpose we gathered the results of the GCM at the four closest grid points to the data during a 5° time range in L_s and 2 h interval in local time.

[47] First we focus the comparison on two parameters mentioned above, in section 3, the electron density at the main ionospheric peak and its altitude. The first one controlled mostly by the magnitude of the UV solar flux, while the second mostly by the atmospheric structure at lower altitudes.

Table 4. Comparison Between the Observed and Simulated Peak Concentration and Altitude, for Each MGS RSS Subset (Measurement-Simulation)

Set Number	$\Delta\overline{e_{peak}}$	$\Delta\overline{z_{peak}}$
1	14.2	–2.6
2	9.7	–2.7
3	37.8	–5.2
4	1.3	–1.8
5	10.3	–0.7
6	13.5	–2.5
7	9.9	–1.8
8	20.2	–0.9
9	23.7	1.5
10	15.3	–1.6
11	14.6	–1.0
12	17.3	2.8

[48] We show in Figures 11 and 12 the comparison between the observed (black crosses) and simulated (red diamonds) electron density at the main ionospheric peak for the MGS RSS data subsets 1–6 and 7–12, respectively, as a function of SZA.

[49] In general, the SZA variability of the electron density at the main peak is well reproduced by the GCM. Particular features such as the peaks at SZA = 71.5 and 74 for the subset #8 or the increase of the electron density for SZA between 71 and 72 for the subset #7 are nicely reproduced by the model. These features that are departures from the theoretical Chapman behavior are produced by the solar variability. A simulation with constant solar flux does not reproduce this small-scale variability, which shows the importance of taking into account the day-to-day solar variability in the simulations of the peak electronic density.

[50] It is also clear that the model tends to underestimate the electron density. This underestimation is approximately constant with SZA within each subset, and its average magnitude is summarized in Table 4. With the exception of subset #3, which we will discuss separately later, the model underestimates the peak concentration between 1 and 23%. A possible reason of this underestimation is the

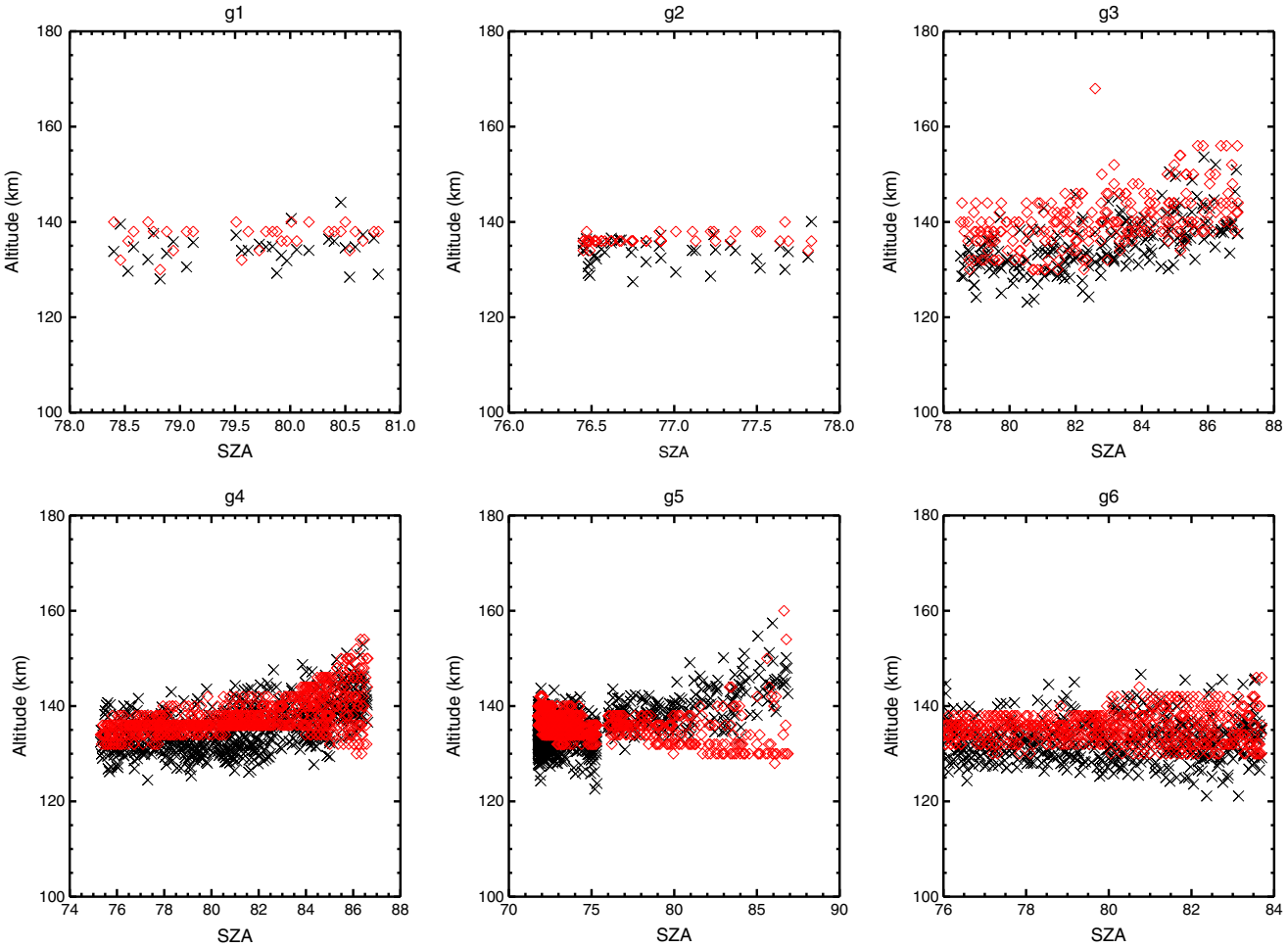

Figure 13. MGS (black crosses) and GCM-simulated (red diamonds) altitude of the main electron peak, as a function of SZA, for the MGS RSS subsets 1–6 described in Table 3.

relatively coarse vertical resolution of the LMD-MGCM in the upper atmosphere (about 7 km). We have performed a short 1 day simulation using an improved vertical resolution of 3 km. The peak electron density is enhanced in average by 8% (with the increase varying between 1 and 17% depending on location and time of the day) with respect to a similar simulation using the nominal vertical grid (to the price of a significant increase in CPU time). This result suggests that at least a significant fraction of the underestimation of the peak electron density is due to the poor vertical resolution in the nominal simulations, with a remaining discrepancy smaller than 10% in average.

[51] There are other assumptions in the model that may introduce biases in the simulations. For example, many reaction rates governing the ionospheric chemistry are affected by high uncertainty. A thorough sensitivity study under all possible values has not been performed yet. We are also using a fixed value for the electronic temperature, based on Viking observations (and affected by important uncertainties), neglecting thus the effects that variations in the electronic temperature can have over the electron density. Another factor that can play a role in this remaining underestimation is the procedure used to include the daily variability of the UV solar flux. As shown in section 2 we are using daily averaged values for this parameter, so that short fluctuations of the solar flux that can introduce some additional variability in the electronic densities are not being considered. As these fluctuations are known to be much stronger in the short wavelengths (extreme UV and X-rays), this effect should specially affect the regions where that spectral range is more important, that is, the ionospheric secondary peak. It is thus unlikely that this short variability of the solar flux may be at the origin of the systematic underestimation of the primary peak. Similarly, although the solar flux is not corrected for the Sun-Mars-Earth angle, this should not produce a systematic underestimation of the electron density.

[52] What about the altitude of the main electronic peak? Figures 13 and 14 show the observed and simulated altitude of the electronic peak for each of the observation groups in Table 3. The model reproduces nicely the observed altitude of the main ionospheric peak, as can also be seen in Table 4. The overall altitude difference is always less than 3 km, that is, less than half the vertical resolution of the GCM. The only exception is subset #3, which is discussed below. There are however some areas with significant differences between the modeled and the measured peak altitude. For subset #12, Figure 14 shows that the difference is concentrated in the high values of SZA: for SZA >85° the observations show an increase of the peak altitude with SZA. Some of the

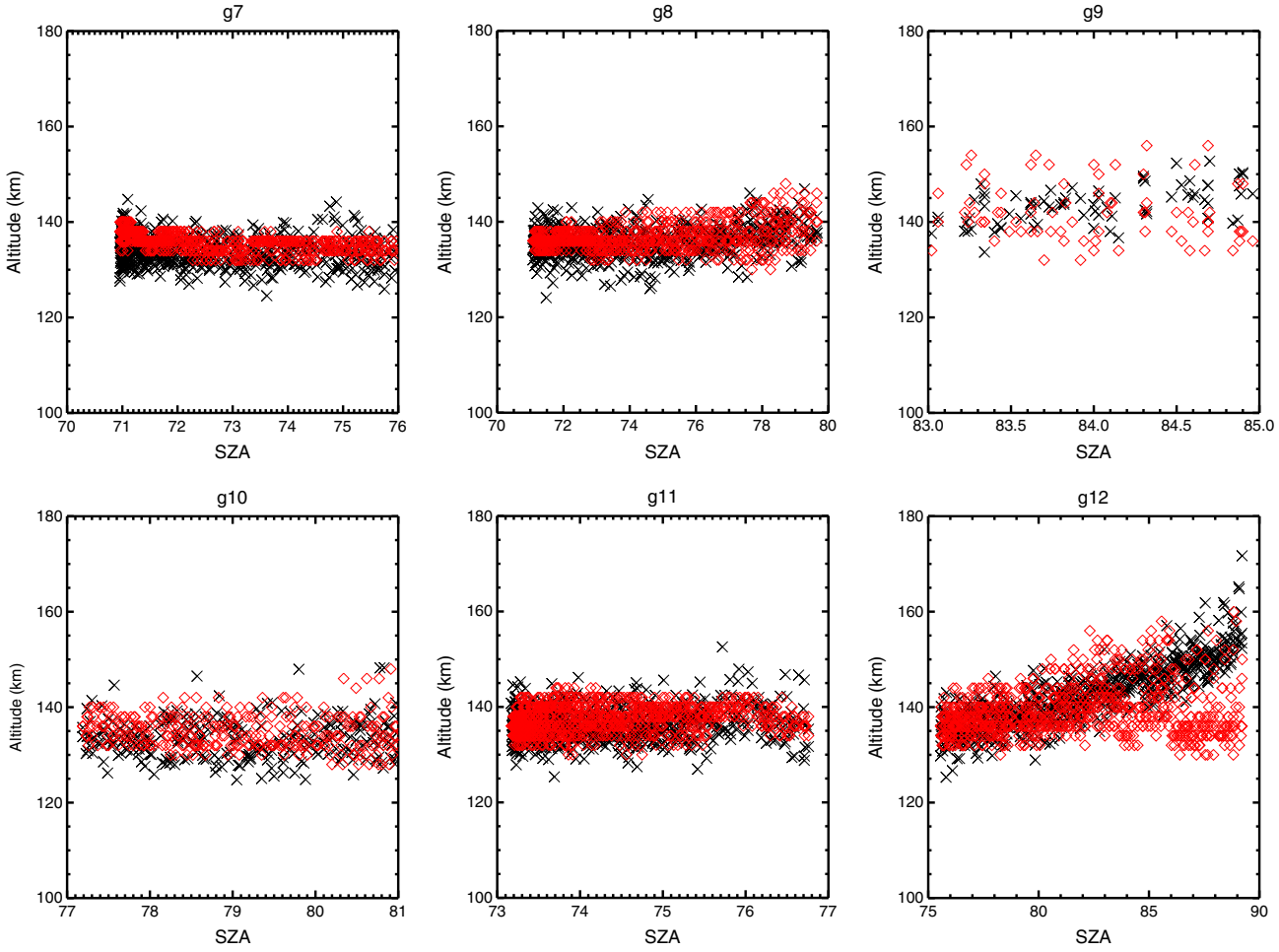

Figure 14. MGS (black crosses) and GCM-simulated (red diamonds) altitude of the main electron peak, as a function of SZA, for the MGS RSS subsets 7–12 described in Table 3.

simulated profiles also show this behavior, but for most of them the peak altitude decreases with increasing SZA. A similar behavior is observed for subset #5. Given that this difference concentrates in the observations with higher SZA, it may indicate that the model is not correctly reproducing the altitude of the main electronic peak close to the terminator. However, for other groups extending to SZA >85°, such as subsets #3 and #4, the observed increase of the peak altitude when approaching the terminator is well reproduced by the model. Apart from these differences, the overall agreement between the simulated and the observed peak altitude is good. Given that the altitude of the peak is determined by the thermal structure in the layers below the peak [*Zou et al.*, 2011], this indicates that the model reproduces correctly the temperatures in the Martian mesosphere/mesopause/lower thermosphere region, in contrast with previous results [*Forget et al.*, 2009; *González-Galindo et al.*, 2009]. This is a direct consequence of the implementation of the new, more physically realistic, 15 μm cooling scheme.

[53] As shown in Figures 11 and 13, as well as in Table 4, there are important differences between the outputs of the model and the observations for subset #3: the main peak concentration difference is higher than 35% and the altitude of the peak is overestimated by the model by more than 5 km. Table 3 shows that the data in subset #3 are obtained in the high latitudes of the southern hemisphere, while for all the other subsets the data correspond to the northern hemisphere. The presence of crustal magnetic fields on the southern hemisphere of Mars is well known [*Acuña et al.*, 2001]. There are previous evidences of perturbations of electronic profiles over magnetized regions. *Withers et al.* [2005] showed that anomalous electronic profiles (those with sharp variations in the electron density) were more likely to occur over regions of strong crustal magnetic field. *Fox and Weber* [2012] found that many of the electronic profiles in subset #3 were extremely disturbed. *Nielsen et al.* [2007] discuss the presence of enhanced peak electron densities at altitudes about 20 km lower than usual over regions with crustal fields, which they attributed to an increase in electron temperature. Very likely, the same effect (which is not taken into account into the model) is producing the underestimation of the peak electronic density and the overestimation of the peak altitude for subset #3 by the model.

[54] The results of the LMD-MGCM can be compared with previous results obtained with a different Martian thermospheric GCM, the MTGCM. *Bougher et al.* [2004] report a decrease in the peak magnitudes from 1.2 to 0.87 $\cdot 10^5$ cm^{-3} (that is, 27.5%) and a rise in the altitude of the peak from

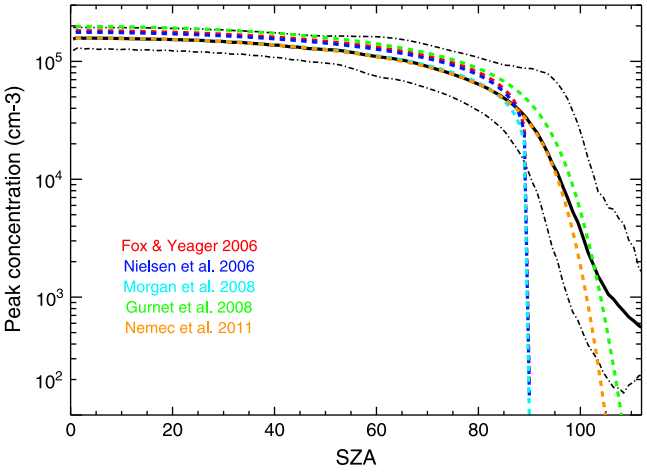

Figure 15. SZA variability of the annual mean peak electron density at daytime predicted by the model (black solid line) plus/minus the standard deviation (black dash-dotted lines) and given by expressions 2 and 3 above (dashed color lines).

131 to 134 km when SZA increases from 74 to 82° in the MTGCM. The LMD-MGCM predicts a decrease of the peak density from about 0.95 to about 0.65 $\cdot 10^5$ cm^{-3} (about 31%) and an increase in the peak altitudes from approximately 130 to 135 km for this SZA variability, as can be seen in Figures 11 and 13, for example, for subsets #4 and #5. This is a very reasonable agreement, considering that both the solar conditions (fixed for solar moderate conditions in the MTGCM and variable according to the observations in the LMD-MGCM) and the season (L_s=90 in the MTGCM, L_s between about 70 and 170 for subsets #4 and #5 in the LMD-MGCM) are not directly comparable. This agreement is in line with the similar thermospheric structure obtained by the MTGCM and the LMD-MGCM during an intercomparison exercise using similar inputs [*González–Galindo et al.*, 2010].

[55] Regarding the comparison with MARSIS data, we focus our study on the SZA variation. MGS data, as all radio occultation measurements, are limited to high values of SZA, and thus the comparison with modeling results can only be made for a limited range of SZA. However, several authors [*Hantsch and Bauer*, 1990; *Gurnett et al.*, 2005; *Withers and Mendillo*, 2005; *Fox and Yeager*, 2006; *Morgan et al.*, 2008; *Sánchez-Cano et al.*, 2013] have overcome this limitation by fitting analytic functions to the observed profiles. For example, supposing a SZA variation of the peak density in agreement with a cosine-like behavior, [*Fox and Yeager*, 2006] propose a variability given by

$$n^e_{\max}(\chi) = A \cdot (\cos(\chi))^a \qquad (2)$$

with A between 1.5 and 2.0 $\cdot 10^5$ cm^{-3}, depending on the solar flux, and a between 0.41 and 0.5.

[56] MARSIS observations are not limited to high SZA, offering a larger range of variability. Different studies have used MARSIS data to characterize the SZA variability of the peak electronic density. So *Nielsen et al.* [2006] analyzed MARSIS results obtained between July and October 2005 and proposed a fit to the SZA variability (for SZA < 85°) given by expression 2, with A = 1.76 and a = 0.476. Similarly, *Morgan et al.* [2008] used a larger MARSIS data set, and proposed the values A = 1.58 and a = 0.5.

[57] Obviously, expression 2 is not appropriate for SZA close to or higher than 90°. For these cases, the cosine of the SZA has to be replaced by the Chapman function:

$$n^e_{\max}(\chi) = B/Ch((\chi, z + R/H))^b \qquad (3)$$

where z is the altitude, R the radius of Mars, and H the scale height.

[58] *Gurnett et al.* [2008] propose the values $B = 1.98 \cdot 10^5$ and b = 0.5, while *Němec et al.* [2011], after analysis of MARSIS results obtained from August 2005 up to the end of 2009 find the values $B = 1.59 \cdot 10^5$ and b = 0.546, with H = 12.16 and z = 124.7.

[59] Figure 15 shows the variability with SZA of the annual mean peak electronic density simulated by the LMD-MGCM and the ones given by expressions 2 and 3 when using the values proposed by the different authors, as summarized above. Let us recall that the solar illumination is computed in the GCM with a proper geometrical ray tracing routine, without approximations like the Chapman function. The model reproduces quite well the observed behavior up to SZA≈ 100°. For SZA between 90 and 100° the slope simulated by the model is in quite good agreement with the expressions based in the Chapman function. For SZA higher than 100° the model predicts a change in the slope that is not observed in the data, corresponding to the moment where NO^+ becomes the dominant ion. It has to be taken into account that the analysis of MARSIS data in *Němec et al.* [2011] is limited to SZA < 100° and that *Gurnett et al.* [2008] report that "for solar zenith angles greater than about 90 degrees the electron densities are highly irregular and extend well above the densities predicted by Chapmans model." We would also like to emphasize the important variability simulated by the model for SZA >80°, which can be as high as almost two orders of magnitude around SZA = 95°. This is surely a response of the ionospheric peak to the natural variability of the lower atmosphere around the day-night transition.

5. Summary and Conclusions

[60] We have included some improvements in the LMD-MGCM that allow it to study the Martian ionosphere in the photochemically dominated region (below about 180–200 km). These improvements include an extension of the previous thermospheric photochemical module [*González–Galindo et al.*, 2005] and a modification of the description of the solar UV flux that allow to take into account its day-to-day variability. Other improvements are a new NLTE 15 μm cooling scheme and a new molecular diffusion module. These last ones are not directly linked to the ionosphere but improve the prediction of the thermal structure and the composition of the upper mesosphere/thermosphere region. A companion paper (J.-Y. Chaufray et al., submitted manuscript, 2013) presents the developments implemented into the LMD-MGCM to study the ionosphere above the photochemical region and studies the impact that the plasma dynamics has over the ionospheric results. They show that the effects of plasma dynamics are important above 180 km in the dayside and contribute to populate the nightside

ionosphere, although their findings do not alter the main results of the photochemically controlled ionosphere presented in this work.

[61] We have presented 3-D simulations of the Martian ionosphere during a full Martian year, which quantify and show that (i) the simulated peak electronic density is affected by the eccentricity of the Martian orbit and (ii) that the seasonal variation of the altitude of the peak is driven by the variability of the altitude of a given pressure level; in other words, by the structure of the whole atmosphere below the peak. These findings are in qualitative agreement with previous observations and modeling results [e.g., *Zou et al.*, 2011; *Bougher et al.*, 2004]. A simulation for a full Martian year incorporating the day-to-day variability of the UV solar flux shows that the variability of the solar flux modulates the seasonal variability due to the eccentricity of the orbit and that the variability of the solar flux due to the solar rotation also affects the peak electronic density by as much as 20%, also in agreement with observations [*Withers and Mendillo*, 2005; *Nielsen et al.*, 2006].

[62] The model predicts the presence of an ionosphere during the night, due to photochemistry only: after sunset, O_2^+ is converted to NO^+, and this ion has a lifetime long enough to survive during the night. The comparison with the scarce observations of the nighttime ionosphere shows that the simulated ionosphere is in agreement with some observations reporting electronic densities around $5{\cdot}10^3$ cm^{-3} for SZA <120° [*Withers et al.*, 2012b], but the model can not explain the presence of areas with enhanced electronic densities of the order of 10^5 cm^{-3} in the deep nightside. This does not necessarily mean a flaw of the model, since we are interested in describing the global ionosphere. Other processes not considered in the model, such as electron precipitation, should be at the origin of these local ionospheric patches. Our results, combined with the measurements of local nighttime enhancements, indicate that below about 140 km there is a nighttime background ionosphere of photochemical rather than transport origin, on top of which enhanced patches may be created locally by electron precipitation or other processes.

[63] The comparison with MGS observations shows that the LMD-MGCM generally underestimates the peak electron density, although the bias is generally lower than about 15%. The SZA variability of the peak electron density is rather well reproduced by the model. Also, the altitude of the electronic peak is very well captured by the model, including the SZA variability, except for a few peculiar features more noticeable at high SZA. This indicates a good simulation of the thermal and density structure of the mesosphere. The comparison with MGS electronic profiles shows also that the electron density at the secondary peak is severely underestimated by the model. This requires an improvement of the description of the extreme UV and the X-rays in the GCM. The comparisons with MARSIS allow to extend the SZA variability of the electron density at the main peak to lower and higher values than those covered by MGS radio science. The SZA variability simulated by the model is in good agreement with that fitted to MARSIS observations up to SZA$\approx$ 100°.

[64] The comparison with the results of another thermospheric/ionospheric GCM, the MTGCM [*Bougher et al.*, 2004] shows that the SZA variability of the peak electron density and the peak altitude is similar in both models.

[65] The LMD-MGCM is being coupled to an exospheric model [*Chaufray et al.*, 2007; *Yagi et al.*, 2012] and to a magnetospheric model [*Modolo et al.*, 2005, 2006] in the frame of a French-funded project called Heliosares. This coupling will allow for a self-consistent description of the different regions forming the Mars upper atmosphere and of its interaction with the solar wind. This approach is particularly interesting with view to the future MAVEN mission, which will greatly improve our knowledge of the upper atmosphere of Mars, and will unveil the different mechanisms coupling the Martian thermosphere, the ionosphere, the exosphere, and the magnetosphere. In particular, MAVEN will provide measurements of the EUV solar flux, and the densities and temperatures of neutrals, ions, and electrons. This set of measurements will allow both to improve the model (for example, by including the measured electronic temperatures) and to test some of its predictions.

[66] **Acknowledgments.** We thank Withers and Lillis for their useful and insightful comments that contributed to improve the quality of the paper. F.G.G. is funded by a CSIC JAE-Doc contract cofinanced by the European Social Fund. F.G.G. and M.A.L.V. thank the Spanish MICINN for funding support through the CONSOLIDER program "ASTROMOL" CSD2009-00038 and through project AYA2011-23552/ESP. This work has also been partially funded by the HELIOSARES Project supported by the ANR (ANR-09-BLAN-0223) and by the ESA-CNES project Mars Climate Database and Physical Models. We thank the members of the teams Mars Upper Atmosphere Network, Heliosares, and Mars Climate Database and Physical models for useful discussions. Solar Irradiance Platform historical irradiances are provided courtesy of W. Kent Tobiska and Space Environment Technologies. These historical irradiances have been developed with partial funding from the NASA UARS, TIMED, and SOHO missions. We thank Ehouarn Millour for developing the tools to process the outputs of the LMD-MGCM and to compare them with observations.

References

Acuña, M. H., et al. (2001), Magnetic field of Mars: Summary of results from the aerobraking and mapping orbits, *J. Geophys. Res.*, *106*, 23,403–23,418, doi:10.1029/2000JE001404.

Angelats i Coll, M., F. Forget, M. A. López-Valverde, and F. González-Galindo (2005), The first Mars thermospheric general circulation model: The Martian atmosphere from the ground to 240 km, *Geophys. Res. Lett.*, *32*, L04201, doi:10.1029/2004GL021368.

Atkinson, R., D. L. Baulch, R. A. Cox, R. F. Hampson, Jr., J. A. Kerr, and J. Troe (1989), Evaluated kinetic and photochemical data for atmospheric chemistry: Supplement III. IUPAC subcommittee on gas kinetic data evaluation for atmospheric chemistry, *J. Phys. Chem. Ref. Data*, *18*, 881–1097, doi:10.1063/1.555832.

Barth, C., A. Stewart, S. Bougher, D. Hunten, S. Bauer, and A. Nagy (1992), *Aeronomy of the Current Martian Atmosphere*, pp. 1054–1089, University of Arizona Press, Tucson.

Bougher, S. W., S. Engel, R. G. Roble, and B. Foster (1999), Comparative terrestrial planet thermospheres 2. Solar cycle variation of global structure and winds at equinox, *J. Geophys. Res.*, *104*, 16,591–16,611, doi:10.1029/1998JE001019.

Bougher, S. W., S. Engel, R. G. Roble, and B. Foster (2000), Comparative terrestrial planet thermospheres 3. Solar cycle variation of global structure and winds at solstices, *J. Geophys. Res.*, *105*, 17,669–17,692, doi:10.1029/1999JE001232.

Bougher, S. W., S. Engel, D. P. Hinson, and J. M. Forbes (2001), Mars Global Surveyor radio science electron density profiles: Neutral atmosphere implications, *Geophys. Res. Lett.*, *28*, 3091–3094, doi:10.1029/2001GL012884.

Bougher, S. W., S. Engel, D. P. Hinson, and J. R. Murphy (2004), MGS radio science electron density profiles: Interannual variability and implications for the Martian neutral atmosphere, *J. Geophys. Res.*, *109*, E03010, doi:10.1029/2003JE002154.

Bougher, S. W., D. J. Pawlowski, and J. R. Murphy (2011), Toward an Understanding of the Time Dependent Responses of the Martian Upper Atmosphere to Dust Storm Events, *AGU Fall Meeting Abstracts*.

Brune, W. H., J. J. Schwab, and J. G. Anderson (1983), Laser magnetic resonance, resonance fluorescence, and resonance absorption studies of the reaction kinetics of O + OH → H + O2, O + HO2 → OH + O2, N + OH → H + NO, and N + HO2 → products at 300 k between 1 and 5 torr, *J. Phys. Chem.*, *87*, 4503–4514.

Chaufray, J. Y., R. Modolo, F. Leblanc, G. Chanteur, R. E. Johnson, and J. G. Luhmann (2007), Mars solar wind interaction: Formation of the Martian corona and atmospheric loss to space, *J. Geophys. Res.*, *112*, E09009, doi:10.1029/2007JE002915.

Chaufray, J.-Y., et al. (2012), Current status on Mars exospheric studies, 39th COSPAR Scientific Assembly, COSPAR Meeting, Mysore, India, 14-22 July, vol. 39, p. 321.

Dickinson, R. E., and E. C. Ridley (1972), Numerical solution for the composition of a thermosphere in the presence of a steady subsolar to antisolar circulation with application to Venus, *J. Atmos. Sci.*, *29*, 1557–1570, doi:10.1175/1520-0469(1972)029<1557:NSFTCO>2.0.CO;2.

Du, M. L., and A. Dalgarno (1990), The radiative association of N and O atoms, *J. Geophys. Res.*, *95*, 12,265–12,268, doi:10.1029/JA095iA08p12265.

Forbes, J. M., S. Bruinsma, and F. G. Lemoine (2006), Solar rotation effects on the thermospheres of Mars and Earth, *Science*, *312*, 1366–1368, doi:10.1126/science.1126389.

Forget, F., F. Hourdin, R. Fournier, C. Hourdin, O. Talagrand, M. Collins, S. R. Lewis, P. L. Read, and J.-P. Huot (1999), improved general circulation models of the Martian atmosphere from the surface to above 80 km, *J. Geophys. Res.*, *104*, 24,155–24,176.

Forget, F., F. Montmessin, J.-L. Bertaux, F. González-Galindo, S. Lebonnois, E. Quémerais, A. Reberac, E. Dimarellis, and M. A. López-Valverde (2009), Density and temperatures of the upper Martian atmosphere measured by stellar occultations with Mars Express SPICAM, *J. Geophys. Res.*, *114*, E01004, doi:10.1029/2008JE003086.

Fox, J. L. (2004), Response of the Martian thermosphere/ionosphere to enhanced fluxes of solar soft X rays, *J. Geophys. Res.*, *109*, A11310, doi:10.1029/2004JA010380.

Fox, J. L., and K. Y. Sung (2001), Solar activity variations of the Venus thermosphere/ionosphere, *J. Geophys. Res.*, *106*, 21,305–21,336, doi:10.1029/2001JA000069.

Fox, J. L., and A. J. Weber (2012), MGS electron density profiles: Analysis and modeling of peak altitudes, *Icarus*, *221*, 1002–1019, doi:10.1016/j.icarus.2012.10.002.

Fox, J. L., and K. E. Yeager (2006), Morphology of the near-terminator Martian ionosphere: A comparison of models and data, *J. Geophys. Res.*, *111*, A10309, doi:10.1029/2006JA011697.

Fox, J. L., and K. E. Yeager (2009), MGS electron density profiles: Analysis of the peak magnitudes, *Icarus*, *200*, 468–479, doi:10.1016/j.icarus.2008.12.002.

Fox, J. L., J. F. Brannon, and H. S. Porter (1993), Upper limits to the nightside ionosphere of Mars, *Geophys. Res. Lett.*, *20*, 1339–1342, doi:10.1029/93GL01349.

Fox, J. L., P. Zhou, and S. W. Bougher (1996), The Martian thermosphere/ionosphere at high and low solar activities, *Adv. Space Res.*, *17*, 203–218, doi:10.1016/0273-1177(95)00751-Y.

González-Galindo, F. (2006), Modelos energeticos, quimicos y dinamicos de la alta atmosfera de Marte, Ph. D. thesis, Universidad de Granada.

González-Galindo, F., M. A. López-Valverde, M. Angelat i Coll, and F. Forget (2005), Extension of a martian general circulation model to thermospheric altitudes: UV heating and photochemical models, *J. Geophys. Res.*, *110*, E09008, doi:10.1029/2004JE002312.

González-Galindo, F., F. Forget, M. A. López-Valverde, M. Angelats i Coll, and E. Millour (2009), A ground-to-exosphere Martian general circulation model: 1. Seasonal, diurnal, and solar cycle variation of thermospheric temperatures, *J. Geophys. Res.*, *114*, E04001, doi:10.1029/2008JE003246.

González-Galindo, F., S. W. Bougher, M. A. López-Valverde, F. Forget, and J. Murphy (2010), Thermal and wind structure of the Martian thermosphere as given by two General Circulation Models, *Planet. Space Sci.*, *58*, 1832–1849, doi:10.1016/j.pss.2010.08.013.

González-Galindo, F., M. A. López-Valverde, F. Forget, and A. Määttäänen (2011), Temperatures in the Martian mesosphere/thermosphere given by a general circulation model, EPSC-DPS Joint Meeting 2011, Nantes, France, 2-7 October, p. 958.

Gurnett, D. A., et al. (2005), Radar soundings of the ionosphere of Mars, *Science*, *310*, 1929–1933, doi:10.1126/science.1121868.

Gurnett, D. A., et al. (2008), An overview of radar soundings of the Martian ionosphere from the Mars Express spacecraft, *Adv. Space Res.*, *41*, 1335–1346, doi:10.1016/j.asr.2007.01.062.

Haberle, R. M., M. M. Joshi, J. R. Murphy, J. R. Barnes, J. T. Schofield, G. Wilson, M. Lopez-Valverde, J. L. Hollingsworth, A. F. C. Bridger, and J. Schaeffer (1999), General circulation model simulations of the Mars Pathfinder atmospheric structure investigation/meteorology data, *J. Geophys. Res.*, *104*, 8957–8974.

Haider, S. A. (1997), Chemistry of the nightside ionosphere of Mars, *J. Geophys. Res.*, *102*, 407–416, doi:10.1029/96JA02353.

Hanson, W. B., and G. P. Mantas (1988), Viking electron temperature measurements: Evidence for a magnetic field in the Martian ionosphere, *J. Geophys. Res.*, *93*, 7538–7544, doi:10.1029/JA093iA07p07538.

Hanson, W. B., S. Sanatani, and D. R. Zuccaro (1977), The Martian ionosphere as observed by the Viking retarding potential analyzers, *J. Geophys. Res.*, *82*, 4351–4363, doi:10.1029/JS082i028p04351.

Hantsch, M. H., and S. J. Bauer (1990), Solar control of the Mars ionosphere, *Planet. Space Sci.*, *38*, 539–542, doi:10.1016/0032-0633(90)90146-H.

Herron, J. (1999), Evaluated chemical kinetics data for reactions of $N(^2D)$ $N(^2P)$, and $N_2(A^3\Sigma_u^+)$ in the gas phase, *J. Phys. Chem. Ref. Data*, *28*, 1453–1483, doi:10.1063/1.556043.

Krasnopolsky, V. A. (2002), Mars' upper atmosphere and ionosphere at low, medium, and high solar activities: Implications for evolution of water, *J. Geophys. Res.*, *107*(E12), 5128, doi:10.1029/2001JE001809.

Lefèvre, S., S. Lebonnois, F. Montmessin, and F. Forget (2004), Three-dimensional modeling of ozone on Mars, *J. Geophys. Res.*, *109*, E07004, doi:10.1029/2004JE002268.

Lillis, R. J., M. O. Fillingim, L. M. Peticolas, D. A. Brain, R. P. Lin, and S. W. Bougher (2009), Nightside ionosphere of Mars: Modeling the effects of crustal magnetic fields and electron pitch angle distributions on electron impact ionization, *J. Geophys. Res.*, *114*, E11009, doi:10.1029/2009JE003379.

Lillis, R. J., M. O. Fillingim, and D. A. Brain (2011), Three-dimensional structure of the Martian nightside ionosphere: Predicted rates of impact ionization from Mars Global Surveyor magnetometer and electron reflectometer measurements of precipitating electrons, *J. Geophys. Res.*, *116*, A12317, doi:10.1029/2011JA016982.

Lollo, A., P. Withers, K. Fallows, Z. Girazian, M. Matta, and P. C. Chamberlin (2012), Numerical simulations of the ionosphere of Mars during a solar flare, *J. Geophys. Res.*, *117*, A05314, doi:10.1029/2011JA017399.

López-Puertas, M., and M. A. López-Valverde (1995), Radiative energy balance of CO2 Non-LTE infrared emissions in the Martian atmosphere, *Icarus*, *114*(1), 113–129, doi:10.1006/icar.1995.1047.

López-Valverde, M. A., F. González-Galindo, and F. Forget (2006), 1-D and 3-D modelling of the upper atmosphere of Mars, in *Proceedings of the Mars Atmosphere: Modelling and Observations*, edited by F. Forget et al., pp. 623, LMD, IAA, AOPP, CNES and ESA, Granada, Spain.

López-Valverde, M. A., F. González-Galindo, and M. López-Puertas (2011), Revisiting the radiative balance of the mesosphere of Mars, in *Proceedings of the Mars Atmosphere: Modelling and Observation*, edited by F. Forget, and E. Millour, pp. 359–362, Paris, France. [Available at http://www-mars.lmd.jussieu.fr/paris2011/program.html.]

McElroy, D., C. Walsh, A. J. Markwick, M. A. Cordiner, K. Smith, and T. J. Millar (2013), The UMIST database for astrochemistry 2012, *Astron. Astrophys.*, *550*, 36–49, doi:10.1051/0004-6361/201220465.

Mendillo, M., S. Smith, J. Wroten, H. Rishbeth, and D. Hinson (2003), Simultaneous ionospheric variability on Earth and Mars, *J. Geophys. Res.*, *108*(A12), 1432, doi:10.1029/2003JA009961.

Modolo, R., G. M. Chanteur, E. Dubinin, and A. P. Matthews (2005), Influence of the solar EUV flux on the Martian plasma environment, *Ann. Geophys.*, *23*, 433–444, doi:10.5194/angeo-23-433-2005.

Modolo, R., G. M. Chanteur, E. Dubinin, and A. P. Matthews (2006), Simulated solar wind plasma interaction with the Martian exosphere: Influence of the solar EUV flux on the bow shock and the magnetic pile-up boundary, *Ann. Geophys.*, *24*, 3403–3410, doi:10.5194/angeo-24-3403-2006.

Morgan, D. D., D. A. Gurnett, D. L. Kirchner, J. L. Fox, E. Nielsen, and J. J. Plaut (2008), Variation of the Martian ionospheric electron density from Mars Express radar soundings, *J. Geophys. Res.*, *113*, A09303, doi:10.1029/2008JA013313.

Nicholson, W. P., G. Gronoff, J. Lilensten, A. D. Aylward, and C. Simon (2009), A fast computation of the secondary ion production in the ionosphere of Mars, *Mon. Not. R. Astron. Soc.*, *400*, 369–382, doi:10.1111/j.1365-2966.2009.15463.x.

Nielsen, E., H. Zou, D. A. Gurnett, D. L. Kirchner, D. D. Morgan, R. Huff, R. Orosei, A. Safaeinili, J. J. Plaut, and G. Picardi (2006), Observations of vertical reflections from the topside Martian ionosphere, *Space Sci. Rev.*, *126*, 373–388, doi:10.1007/s11214-006-9113-y.

Nielsen, E., et al. (2007), Local plasma processes and enhanced electron densities in the lower ionosphere in magnetic cusp regions on Mars, *Planet. Space Sci.*, *55*, 2164–2172, doi:10.1016/j.pss.2007.07.003.

Němec, F., D. D. Morgan, D. A. Gurnett, F. Duru, and V. Truhlík (2011), Dayside ionosphere of Mars: Empirical model based on

data from the MARSIS instrument, *J. Geophys. Res.*, *116*, E07003, doi:10.1029/2010JE003789.

Pätzold, M., S. Tellmann, B. Häusler, D. Hinson, R. Schaa, and G. L. Tyler (2005), A sporadic third layer in the ionosphere of Mars, *Science*, *310*, 837–839, doi:10.1126/science.1117755.

Rohrbaugh, R. P., J. S. Nisbet, E. Bleuler, and J. R. Herman (1979), The effect of energetically produced O2+ on the ion temperatures of the Martian thermosphere, *J. Geophys. Res.*, *84*, 3327–3338, doi:10.1029/JA084iA07p03327.

Safaeinili, A., W. Kofman, J. Mouginot, Y. Gim, A. Herique, A. B. Ivanov, J. J. Plaut, and G. Picardi (2007), Estimation of the total electron content of the Martian ionosphere using radar sounder surface echoes, *Geophys. Res. Lett.*, *34*, L23204, doi:10.1029/2007GL032154.

Sánchez-Cano, B., S. M. Radicella, M. Herraiz, O. Witasse, and G. Rodríguez-Caderot (2013), NeMars: An empirical model of the Martian dayside ionosphere based on Mars Express MARSIS data, *Icarus*, *225*, 236–247, doi:10.1016/j.icarus.2013.03.021.

Sander, S. P., et al. (2011), *Chemical kinetics and photochemical data for the use in atmospheric studies. Evaluation number 17, JPL publication 10-6*, Jet Propulsion Laboratory, Pasadena. http://jpldataeval.jpl.nasa.gov.

Schunk, R., and A. Nagy (2009), *Ionospheres: Physics, plasma physics, and chemistry* (2nd edn), Cambridge atmospheric and space science series, Cambridge University Press, Cambridge, U. K.

Spiga, A., F. González-Galindo, M.-Á. López-Valverde, and F. Forget (2012), Gravity waves, cold pockets and CO_2 clouds in the Martian mesosphere, *Geophys. Res. Lett.*, *39*, L02201, doi:10.1029/2011GL050343.

Tobiska, W. K., and S. D. Bouwer (2006), New developments in SOLAR2000 for space research and operations, *Adv. Space Res.*, *37*, 347–358, doi:10.1016/j.asr.2005.08.015.

Tsang, W., and R. F. Hampson (1986), Chemical Kinetic Data Base for Combustion Chemistry. Part I. Methane and Related Compounds, *J. Phys. Chem. Ref. Data*, *15*, 1087–1279, doi:10.1063/1.555759.

Withers, P. (2009), A review of observed variability in the dayside ionosphere of Mars, *Adv. Space Res.*, *44*, 277–307, doi:10.1016/j.asr.2009.04.027.

Withers, P., and M. Mendillo (2005), Response of peak electron densities in the Martian ionosphere to day-to-day changes in solar flux due to solar rotation, *Planet. Space Sci.*, *53*, 1401–1418, doi:10.1016/j.pss.2005.07.010.

Withers, P., M. Mendillo, H. Rishbeth, D. P. Hinson, and J. Arkani-Hamed (2005), Ionospheric characteristics above Martian crustal magnetic anomalies, *Geophys. Res. Lett.*, *32*, L16204, doi:10.1029/2005GL023483.

Withers, P., M. Mendillo, D. P. Hinson, and K. Cahoy (2008), Physical characteristics and occurrence rates of meteoric plasma layers detected in the Martian ionosphere by the Mars Global Surveyor Radio Science Experiment, *J. Geophys. Res.*, *113*, A12314, doi:10.1029/2008JA013636.

Withers, P., et al. (2012a), A clear view of the multifaceted dayside ionosphere of mars, *Geophys. Res. Lett.*, *39*, L18202, doi:10.1029/2012GL053193.

Withers, P., M. O. Fillingim, R. J. Lillis, B. HäUsler, D. P. Hinson, G. L. Tyler, M. PäTzold, K. Peter, S. Tellmann, and O. Witasse (2012b), Observations of the nightside ionosphere of Mars by the Mars Express radio science experiment (MaRS), *J. Geophys. Res.*, *117*, A12307, doi:10.1029/2012JA018185.

Yagi, M., F. Leblanc, J. Y. Chaufray, F. Gonzalez-Galindo, S. Hess, and R. Modolo (2012), Mars exospheric thermal and non-thermal components: Seasonal and local variations, *Icarus*, *221*, 682–693, doi:10.1016/j.icarus.2012.07.022.

Zhang, M. H. G., J. G. Luhmann, and A. J. Kliore (1990), An observational study of the nightside ionospheres of Mars and Venus with radio occultation methods, *J. Geophys. Res.*, *95*, 17,095–17,102, doi:10.1029/JA095iA10p17095.

Zou, H., R. J. Lillis, J. S. Wang, and E. Nielsen (2011), Determination of seasonal variations in the Martian neutral atmosphere from observations of ionospheric peak height, *J. Geophys. Res.*, *116*, E09004, doi:10.1029/2011JE003833.